



# Contrasting air pollution responses to hourly varying anthropogenic NO<sub>x</sub> emissions in the contiguous United States

Madankui Tao<sup>1,2,3</sup>, Arlene M. Fiore<sup>1,2</sup>, Louisa K. Emmons<sup>4</sup>, Jeffery R. Scott<sup>1</sup>, Gabriele G. Pfister<sup>4</sup>, Duseong S. Jo<sup>5</sup>, and Wenfu Tang<sup>4</sup>

<sup>1</sup>Earth Atmospheric and Planetary Sciences, Massachusetts Institute of Technology, Cambridge, MA, 02139, USA

<sup>2</sup>Lamont-Doherty Earth Observatory, Columbia University, Palisades, NY, 10964, USA

<sup>3</sup>Department of Earth and Environmental Sciences, Columbia University, New York, NY, 10027, USA

<sup>4</sup>Atmospheric Chemistry Observations & Modeling Laboratory, National Center for Atmospheric Research, Boulder, CO, 80301, USA

<sup>5</sup>Department of Earth Science Education, Seoul National University, Gwanak-gu, Seoul, 08826, South Korea

**Correspondence:** Madankui Tao (taoma528@mit.edu)

Received: 3 September 2025 – Discussion started: 3 November 2025

Revised: 21 February 2026 – Accepted: 22 April 2026 – Published: 18 May 2026

**Abstract.** Some global atmospheric chemistry modeling applications assume that intra-month variability in anthropogenic emissions averages out at monthly timescales. To systematically quantify the impacts of resolving daily and hourly emissions, we use a global model with a refined  $\sim 14$  km resolution over the contiguous United States (CONUS; MUSICAv0) and a regional CONUS inventory for July 2018. Switching from daily to hourly nitric oxide (NO) emissions (typically higher during the day and lower at night) yields contrasting spatial responses in nitrogen oxides (NO<sub>x</sub>  $\equiv$  NO + nitrogen dioxide (NO<sub>2</sub>)) and ozone (O<sub>3</sub>) concentrations in the western versus eastern CONUS and in urban versus rural areas. Neglecting hourly variations in CONUS NO emissions leads to grid-cell level discrepancies in monthly mean surface O<sub>3</sub> concentrations of  $-22\%$  to  $+11\%$  ( $-7$  to  $+5$  ppb) and surface NO<sub>2</sub> of  $-49\%$  to  $+86\%$  ( $-1$  to  $+8$  ppb), with tropospheric NO<sub>2</sub> columns showing similar spatial patterns ( $-12\%$  to  $+56\%$ ). While comparable in magnitude to a uniform 30% NO emission reduction (grid-cell level surface O<sub>3</sub> differences of  $-12\%$  to  $+9\%$ ,  $-7$  to  $+3$  ppb), the spatial response patterns differ with location-specific timing of emissions and meteorology. For example, Los Angeles shows higher morning NO<sub>x</sub> concentrations and stronger NO<sub>x</sub>-saturated O<sub>3</sub> suppression relative to New York City. A simple scaling analysis suggests that neglecting hourly emissions variability can bias NO<sub>x</sub> emissions inferred from monthly mean tropospheric NO<sub>2</sub> columns, with absolute relative differences ranging from  $\sim 1\%$  to  $\sim 56\%$  within individual model grid cells.

## 1 Introduction

Exposure to ground-level ozone (O<sub>3</sub>) pollution can intensify the risk of respiratory and cardiovascular diseases (Dedoussi et al., 2020; Di et al., 2017a, b; Strosnider et al., 2019). However, understanding the drivers of surface O<sub>3</sub> variations is challenging due to its formation through nonlinear photochemical reactions involving its precursors: nitrogen ox-

ides (NO<sub>x</sub>), volatile organic compounds (VOCs), and carbon monoxide (CO). Nonlinear O<sub>3</sub> production sensitivity to NO<sub>x</sub> and VOCs is commonly described in terms of three photochemical regimes: the NO<sub>x</sub>-saturated regime, in which O<sub>3</sub> concentrations increase with reductions in NO<sub>x</sub> or increases in VOCs; the NO<sub>x</sub>-sensitive regime, in which O<sub>3</sub> increases with increasing NO<sub>x</sub> but shows limited response to VOCs; and a transitional regime, where O<sub>3</sub> responds similarly to

changes in both precursors (Kleinman, 1994, 2005; Sillman, 2003; Sillman and He, 2002; Tonnesen and Dennis, 2000). Air quality models are often applied to bridge observational gaps, attribute pollution sources, and quantify O<sub>3</sub> sensitivity to precursor emissions. Their reliability depends in part on the accuracy of the anthropogenic emissions driving the simulations. We focus here on how temporal changes in emissions influence pollutant concentrations, highlighting the importance of accounting for diurnal variability when interpreting or inferring emissions from observed concentrations, and vice versa. Below, we specifically address the question: How does the temporal resolution (monthly, daily, or hourly) of anthropogenic emissions inventories affect model simulated concentrations and spatiotemporal variability of O<sub>3</sub> and its precursors across the contiguous United States (CONUS)?

Recent advances in global atmospheric chemistry models include the introduction of variable resolution options for continental-scale air pollution modeling (e.g., Wang et al., 2004; Goto et al., 2020; Krol et al., 2005), with higher horizontal resolution generally improving model alignment with observations (e.g., Schwantes et al., 2022; Jo et al., 2023; Yu et al., 2016). The variable resolution option provides high resolution over specified regions while avoiding the need for boundary conditions required by regional models, enabling studies of local-to-global influences on regional air pollution within a framework of globally consistent dynamics, physics, and chemistry. Version 0 of the Multi-Scale Infrastructure for Chemistry and Aerosols (MUSICAv0) is a configuration of the Community Atmosphere Model with chemistry (CAM-chem) and horizontal regional mesh refinement using the spectral element dynamical core (Pfister et al., 2020). Previous applications of MUSICAv0 have investigated O<sub>3</sub> photochemistry in the southeast U.S. (Schwantes et al., 2022), the effects of wildfires (Tang et al., 2022, 2023b, 2025), and air quality in Africa (Tang et al., 2023a) and South Korea (Jo et al., 2023).

Global atmospheric chemistry models often do not represent daily and diurnal variations in anthropogenic emissions. Instead, monthly averaged inventories are used, avoiding the challenges associated with obtaining high temporal resolution inventories in some regions and the substantial disk storage required for a model to read in hourly emissions online. While some models incorporate detailed diurnal and day-of-week variations directly in the input emissions files by providing all dates and hours, as we implement below, others apply geographically varying scaling factors for selected regions and species (Keller et al., 2014; Lin et al., 2021). Prior regional chemical transport model (CTM) studies have examined the sensitivity of simulated surface air pollutant concentrations to sub-daily variations in anthropogenic emissions across a range of modeling frameworks (e.g., WRF-CMAQ, CHIMERE). These studies show that the temporal allocation of emissions can influence pollutant concentrations and their daytime-nighttime contrasts, particularly for species with strong diurnal variability such as NO<sub>x</sub>

and O<sub>3</sub> (e.g., Guevara et al., 2025; Jo et al., 2023; Menut et al., 2012; Shen et al., 2023). Despite their increasing relevance for interpreting retrievals from geostationary satellite missions such as Tropospheric Emissions: Monitoring of Pollution (TEMPO), a systematic quantification of how hourly anthropogenic emissions affect daily or monthly averages of both surface and column concentrations over the United States remains lacking.

We show below that neglecting hourly variations in anthropogenic emissions can lead to discrepancies in simulated monthly mean NO<sub>x</sub> and O<sub>3</sub> concentrations, ranging from −49 % to +86 % for NO<sub>2</sub> and from −22 % to +11 % for O<sub>3</sub> within individual model grid cells, and in emissions inferred from satellite retrievals. We select July 2018 as a representative summer month for our analysis because it coincides with the availability of TROPOspheric Monitoring Instrument (TROPOMI) observations, which began in May 2018. Our summer focus reflects active photochemistry during this season, when surface O<sub>3</sub> concentrations are typically highest and most likely to exceed the U.S. National Ambient Air Quality Standards (NAAQS) (Tao et al., 2022, 2025). Section 2 describes the MUSICAv0 model framework and simulation design that we use to examine the impact of diurnal variations in emissions on concentrations (Sect. 2.1). Section 3 evaluates the model simulations against surface measurements of trace gases (O<sub>3</sub>, NO<sub>2</sub>, CO, and sulfur dioxide (SO<sub>2</sub>)) and fine particulate matter (PM<sub>2.5</sub>), as well as TROPOMI satellite retrievals of tropospheric NO<sub>2</sub> and HCHO columns and total vertical column CO. After briefly describing these observational datasets (Sect. 3.1), we assess the impact of using a regional emission inventory (Sect. 3.2) and incorporating hourly emission variations (Sect. 3.3). We then examine diurnal and weekday-weekend patterns in pollutant concentrations (Sect. 3.4). Section 4 isolates the effects of resolving hourly nitric oxide (NO) emissions. We first examine west-to-east contrasts in surface pollutant responses (Sect. 4.1) before discussing urban case studies in Los Angeles and New York City (Sect. 4.2). We then present a simplified analysis to quantify the impacts of neglecting diurnal emission variability on NO<sub>x</sub> emissions inferred from monthly mean polar-orbiting satellite retrievals (Sect. 4.3). Section 5 summarizes the key findings and discusses their implications.

## 2 Model Description and Simulations

We use a standard configuration of MUSICAv0 that features a  $\sim 14\text{ km} \times 14\text{ km}$  refined grid for the CONUS (“ne0CONUSne30x8”), which has been shown to better represent observed surface concentrations of O<sub>3</sub> and its precursors such as NO<sub>x</sub> and CO compared to the  $\sim 100\text{ km}$  (“ne30”) global horizontal resolution (Schwantes et al., 2022). We conduct all simulations for the year 2018. The MUSICAv0 atmospheric model is a configuration of CAM6-

chem, version 6 of the Community Atmosphere Model (CAM6), which is a component of the Community Earth System Model (CESM) version 2.2 (Danabasoglu et al., 2020; Emmons et al., 2020). The CAM meteorology is nudged to the 3-hourly Modern-Era Retrospective analysis for Research and Applications Version 2 (MERRA2) meteorology (Gelaro et al., 2017). The MUSICAv0 (CESM2/CAM6-chem) model simulations use 32 vertical layers from the surface up to about 1 hPa ( $\sim 45$  km) (Tilmes et al., 2019).

In the standard simulation (hereafter, *BASE*), we use MOZART-TS1 troposphere-stratosphere chemistry (Emmons et al., 2020; Tilmes et al., 2019), with monthly Copernicus Atmosphere Monitoring Service (CAMS-GLOB-ANT) v5.1 for global anthropogenic emissions (Eskes et al., 2021) and daily Fire INventory from NCAR (National Center for Atmospheric Research) (FINN) v2.5 (Wiedinmyer et al., 2023) for biomass burning emissions. Biogenic emissions of VOCs and CO are calculated online in the land component of CESM (Lawrence et al., 2019) based on the Model of Emissions of Gases and Aerosols from Nature (MEGAN) version 2.1 (Guenther et al., 2012). Additional emissions, such as soil NO<sub>x</sub>, oceanic CO, and hydrocarbons, are taken from the POET inventory (Granier et al., 2005). Dry deposition is calculated interactively from parameterizations using meteorology and biophysics from the coupled atmosphere and land models (Emmons et al., 2020). We prescribe latitudinally varying fixed mixing ratio lower boundary conditions for carbon dioxide (CO<sub>2</sub>), methane (CH<sub>4</sub>), nitrous oxide (N<sub>2</sub>O), and other well-mixed greenhouse gases for 2018 according to the ScenarioMIP SSP5-8.5 pathway from the Coupled Model Intercomparison Project Phase 6 (CMIP6) (Meinshausen et al., 2017).

The *BASE* simulation covers the period from January to September 2018. Previous CESM2.2 studies have employed nudging relaxation times of 50 h (Schwantes et al., 2020), 12 h (Tang et al., 2023b), and 6 h (Tang et al., 2022). For the *BASE* simulation, we adopt an intermediate option of 12 h nudging relaxation time as recommended for driving the model with 3 h meteorology fields (Davis et al., 2022; Gaubert et al., 2020; Schwantes et al., 2022). Only “*T*” (air temperature), “*U*” (zonal wind velocity), and “*V*” (meridional wind velocity) are nudged. We conduct short perturbation simulations relative to the *BASE* case from 1–5 July 2018 (Table S1 in the Supplement) to test the model sensitivity to changes in total anthropogenic and biogenic emissions, as well as to an alternative chemical mechanism with more detailed isoprene and terpene chemistry (Schwantes et al., 2022) (Sect. S1; Figs. S1 and S2a). We also confirm that using 12 h nudging maintains consistent meteorological conditions (*T*, *U*, *V*) across emission scenarios, ensuring that weather variability does not substantially affect conclusions drawn by differencing simulations (Sect. S2; Fig. S3). For our July 2018 sensitivity simulations (Table 1), we save hourly mean diagnostics of meteorological conditions, con-

centrations of major trace gases and aerosols, deposition fluxes, as well as O<sub>3</sub> production and loss rates.

### Modifications to the CONUS Anthropogenic Emissions Inventory

The standard global emission inventory in MUSICAv0 is CAMS-GLOB-ANT, which provides monthly averages for 36 emitted compounds within 17 sectors at a spatial resolution of  $0.1^\circ \times 0.1^\circ$  (latitude  $\times$  longitude) (Soulie et al., 2024). Here, we use CAMS-GLOB-ANT version 5.1 (Eskes et al., 2021), which combines the Emissions Database for Global Atmospheric Research (EDGAR) v5 (Crippa et al., 2019) up to 2015 with the Community Emissions Data System (CEDS) (McDuffie et al., 2020) to extend emissions from 2016 to 2021. To evaluate the sensitivity of simulated air pollutant concentrations to the temporal resolution of anthropogenic emissions, we replace the global CAMS-GLOB-ANT baseline inventory with the U.S. Environmental Protection Agency (EPA) National Emissions Inventory (NEI) over the CONUS, which provides more detailed (higher spatial resolution; hourly-varying) regional emissions. We then conduct a series of simulations that differ only in the temporal resolution of NEI emissions (monthly, daily, or hourly) to isolate the model response to the timing of emissions while holding the total emissions for July constant.

The U.S. NEI includes emissions of criteria pollutants, precursors, and hazardous air pollutants (U.S. Environmental Protection Agency, 2024). The NEI is updated every three years and constructed through the Emissions Inventory System (EIS), which collects and integrates data primarily provided by State, Local, and Tribal air agencies. We first process the 2017 NEI (U.S. Environmental Protection Agency, 2022), the most recent pre-COVID inventory available at the time of this study, to generate hourly emissions on a  $\sim 0.1^\circ \times 0.1^\circ$  grid over the CONUS (Sect. S3) using sector-specific diurnal profiles to capture within-day as well as day-to-day variations. The 2017 hourly NEI data are then shifted by one calendar day so that the weekday-weekend cycle matches the 2018 calendar and re-gridded (mass-conserving) to the unstructured ne0CONUSne30x8 horizontal resolution using NCAR-developed tools (National Center for Atmospheric Research, 2022a, b). All subsequent references to NEI in this study refer to this adjusted product unless otherwise noted.

Switching from CAMS-GLOB-ANT v5.1 to monthly mean NEI emissions yields widespread decreases in most emitted species across the CONUS, particularly for NO and CO (Fig. S4c). Changes in anthropogenic VOC emissions are also evident (Fig. S4c), but their magnitude remains small compared with biogenic VOC emissions (compare Fig. S5 with Fig. S4a–b; see Sect. S4 for the full list of emitted VOC species). We verified that hourly NEI emissions are read by MUSICAv0 in UTC time with the prescribed diurnal and

**Table 1.** MUSICAv0 *BASE* configuration (January–September 2018) and U.S. Environmental Protection Agency (EPA) National Emissions Inventory (NEI) sensitivity simulations with modifications (Sect. 2.1) to anthropogenic emissions (July 2018). The last two columns indicate whether each simulation includes day-specific weekday-weekend and/or diurnal variability in anthropogenic emissions.

Simulation ID	Anthropogenic Emissions Perturbation		
	Details	Weekday-weekend Variability	Diurnal Variability
<i>BASE</i>	Monthly CAMS-GLOB-ANT v5.1 anthropogenic emissions everywhere	No	No
<i>NEI_monthly</i>	Monthly NEI data replaces the CAMS-GLOB-ANT v5.1 anthropogenic emissions over the CONUS	No	No
<i>NEI_monthly_m30anthroNO</i>	Same as <i>NEI_monthly</i> , but anthropogenic NO emissions are reduced by 30 %	No	No
<i>NEI_monthly_m30anthroVOC</i>	Same as <i>NEI_monthly</i> , but anthropogenic VOC emissions are reduced by 30 %	No	No
<i>NEI_hourly</i>	Hourly NEI data replaces anthropogenic emissions over the CONUS	Yes	Yes
<i>NEI_hourly_NO</i>	Same as <i>NEI_monthly</i> , but with hourly NO emissions from the NEI over the CONUS	Yes (NO only)	Yes (NO only)
<i>NEI_daily_NO</i>	Same as <i>NEI_monthly</i> , but with daily-mean NO emissions from the NEI over the CONUS	Yes (NO only)	No

weekday-weekend variability preserved in local time at the grid-cell level (Sect. S3; Figs. S6 and S7).

To assess the impact of using an alternate anthropogenic emissions inventory and different temporal resolutions of emissions, we conduct four one-month simulations (Table 1): (1) monthly NEI data replace CAMS-GLOB-ANT v5.1 emissions over the CONUS, with CAMS monthly means retained elsewhere (*NEI\_monthly*); (2) as in *NEI\_monthly* but hourly NEI emissions are applied for all species over the CONUS (*NEI\_hourly*); (3) as in *NEI\_monthly*, but only NO is emitted hourly (*NEI\_hourly\_NO*); (4) as in *NEI\_monthly*, but NO emissions vary daily and thus include weekday-weekend differences (*NEI\_daily\_NO*). Here, anthropogenic NO<sub>x</sub> emissions are provided as NO, the predominant emitted form of NO<sub>x</sub>. Hourly NEI emissions (*NEI\_hourly* and *NEI\_hourly\_NO*) include day-specific diurnal variability (and therefore distinguish between weekdays and weekends), whereas *NEI\_daily\_NO* removes within-day (diurnal) variability (Table 1). To summarize: the *NEI\_monthly* vs. *BASE* comparison isolates the effect of changing emission inventories; *NEI\_hourly* vs. *NEI\_monthly* assesses the influence of adding sub-monthly (daily and diurnal) variability for all anthropogenic emissions, *NEI\_daily\_NO* vs. *NEI\_monthly* isolates the effect of weekday-weekend differences in NO emissions, and *NEI\_hourly\_NO* vs. *NEI\_daily\_NO* isolates the effect of the diurnal changes in NO emission.

We conduct two additional one-month simulations using the *NEI\_monthly* case as the reference to ana-

lyze the O<sub>3</sub> production regime under idealized perturbations to anthropogenic NO<sub>x</sub> and VOC emissions. In one simulation, we reduce anthropogenic NO emissions by 30 % (*NEI\_monthly\_m30anthroNO*) and in another we reduce anthropogenic VOC emissions by 30 % (*NEI\_monthly\_m30anthroVOC*) (Table 1). These additional sensitivity simulations provide context for those incorporating the more nuanced changes in the temporal resolution of anthropogenic emissions (Sect. S4).

### 3 Evaluating the Sensitivity of Simulated Air Pollution to Emission Inventory Choice and Temporal Resolution

To account for regional variation, we divide the CONUS into six regions: West Coast, Mountain, Midwest, Southwest, Northeast, and Southeast (Fig. 1). For each region, Fig. 2 compares modeled (Sect. 2) and observed (Sect. 3.1) July mean surface concentrations of NO<sub>2</sub>, O<sub>3</sub>, and CO, as well as vertical column densities of tropospheric NO<sub>2</sub> and HCHO and total CO (Sect. 3.2; additional details are in Table S2). We evaluate the model spatial representation of the observations using Spearman's rank correlation coefficient ( $r_s$ ) and mean bias error (MBE), calculated from monthly mean values at all grid cells within the selected domain. Detailed statistics for July mean values, including the absolute and relative differences in both MBE and root mean square error (RMSE), are provided in Table S2. Our primary focus is on

O<sub>3</sub> and its precursors, though for completeness we include evaluations of surface SO<sub>2</sub> and PM<sub>2.5</sub> in Sect. S5 and Table S3. Urban case studies are used to illustrate these effects at the local scale (e.g., a single model grid cell), where responses are most pronounced and easiest to interpret (Fig. 4).

### 3.1 Observational Datasets for Model Evaluation

We use measurements collected from State and Local Air Monitoring Stations (SLAMS) that are reported to the U.S. EPA Air Quality System (AQS) for trace gases (O<sub>3</sub>, NO<sub>2</sub>, CO, and SO<sub>2</sub>) and PM<sub>2.5</sub> concentrations (Table S4), downloaded from the AQS AirData portal ([https://aqsweb.airdata/download\\_files.html](https://aqsweb.airdata/download_files.html), last access: 1 August 2023). To compare MUSICAv0 surface simulations with SLAMS surface measurements, we identify the closest model grid cell based on the latitude and longitude of the SLAMS monitors. We then align hourly concentrations in local time from SLAMS with MUSICAv0 for each species across all CONUS monitors. A limitation of this evaluation is that most SLAMS sites are in urban areas and are influenced by localized effects that cannot be fully resolved by the model at 14 km resolution, which may affect the representativeness of site-level comparisons. The locations of SLAMS used in this study for each species, along with their distribution across CONUS regions and the number of monitors within selected urban grid cells, are shown in Fig. S8.

We select six monitoring stations as examples to examine diurnal patterns at individual sites (Table S5), chosen based on their proximity to major city centers across the CONUS and the availability of continuous NO<sub>2</sub> and O<sub>3</sub> measurements throughout July 2018. Nearby stations with similar diurnal behavior were excluded to avoid redundancy. We do not average across sites as we prefer to preserve distinct local features given differences in monitor availability across cities (Fig. S8).

We also use retrievals from TROPOMI, a nadir-viewing shortwave spectrometer aboard the Sentinel 5 Precursor (S5P) satellite launched in 2017 and operational in 2018. We compare tropospheric vertical column densities (VCD<sub>Trop</sub>) of NO<sub>2</sub> (5.5 km × 3.5 km) and HCHO (5.5 km × 3.5 km), along with total vertical column densities (VCD<sub>Total</sub>) of CO (5.5 km × 7 km) retrieved from TROPOMI (RPRO Version 02.04.00; last access: 1 December 2023). We select pixels with quality assurance greater than 0.75 (Table S4), which largely excludes cloudy and partly cloudy pixels (van Geffen et al., 2020; Lange et al., 2023). We re-grid the column densities and corresponding averaging kernels (AKs) to a horizontal resolution of 0.15° × 0.15°, slightly coarser than that of the model simulations over the CONUS (approximately 0.125°). TROPOMI uses *a priori* profiles derived from the TM5-MP global chemistry transport model (Myriokefalitakis et al., 2020), the massively parallel (MP) version of the Tracer Model version 5 (TM5), to simulate the vertical distribution of NO<sub>2</sub>, HCHO, and CO, which are pro-

vided as supplementary data with the Level-2 products. The TM5-MP model provides data at a 1° × 1° horizontal resolution for the troposphere and upper troposphere-lower stratosphere on 34 hybrid sigma-pressure levels from the surface to approximately 0.1 hPa for retrieving the VCD<sub>Trop</sub> of NO<sub>2</sub> and HCHO (Williams et al., 2017). The CO total column density retrievals are based on 50 hybrid sigma-pressure levels from TM5-MP.

To compare modeled column densities with TROPOMI retrievals, we mass conservatively re-grid the hourly MUSICAv0 HCHO, NO<sub>2</sub>, CO, and meteorological variables to a 0.15° × 0.15° finite volume grid. We calculate the average between 01:00 and 02:00 p.m. LT (to approximate 01:30 p.m. values) for each region and apply the TROPOMI AKs, linearly interpolated vertically to the MUSICAv0 vertical resolution, to ensure a consistent application of AKs across all MUSICAv0 sensitivity simulations when calculating modeled VCD<sub>Trop</sub> of NO<sub>2</sub> and HCHO and VCD<sub>Total</sub> of CO. Our interpolation of the TROPOMI AKs to the MUSICAv0 vertical grid generally preserves their vertical structure without introducing unphysical smoothing (Fig. S9). We use the tropopause height diagnosed from the model simulations. Applying AKs to the modeled column enables a more consistent comparison between model simulations and satellite retrievals by accounting for the vertical sensitivity of the satellite instrument. We compare daily 01:30 p.m. VCD<sub>Trop</sub> or VCD<sub>Total</sub> values across individual grid cells, matching each valid retrieval to the nearest model grid cell. Reported averages include only grid cells with valid retrievals after quality filtering.

### 3.2 Choice of Monthly Emission Inventory (*BASE* vs. *NEI\_monthly*) Influences Simulated Air Pollution

We focus on region-specific comparisons with observations across the CONUS (Fig. 2; Tables S2 and S3), as substantial spatial variation suggests that national-level summaries may obscure important regional differences. Across the six CONUS regions, spatial correlations between observed and modeled surface concentrations in the *BASE* simulation (with the global CAMS-GLOB-ANT emissions) are stronger for NO<sub>2</sub> and O<sub>3</sub> ( $r_s$  typically > 0.5) than for CO ( $r_s = 0.10$ – $0.36$ ) (Fig. 2a; Table S2). Modeled surface concentrations of NO<sub>2</sub> are biased high by 22%–40% (2–5 ppb) in all regions except the Mountain region, which shows an average low bias of 18% (1 ppb). Modeled July mean surface O<sub>3</sub> concentrations are overestimated by 11%–29% (6–13 ppb). Surface CO is underestimated by 17%–87% (27–140 ppb) compared to SLAMS across all regions. Modeled July mean VCDs (Fig. 2b; Table S2) correlate spatially with TROPOMI NO<sub>2</sub> VCD<sub>Trop</sub> ( $r_s = 0.65$ – $0.85$ ) and HCHO VCD<sub>Trop</sub> ( $r_s = 0.60$ – $0.92$ ), though the correlation is weak for CO VCD<sub>Total</sub> ( $r_s = 0.11$ – $0.53$ ). Modeled NO<sub>2</sub> VCD<sub>Trop</sub> is underestimated by 34%–48% ( $\sim 3 \times 10^{14}$  molec. cm<sup>-2</sup>), while HCHO VCD<sub>Trop</sub> is overestimated by 15%–24% (1–

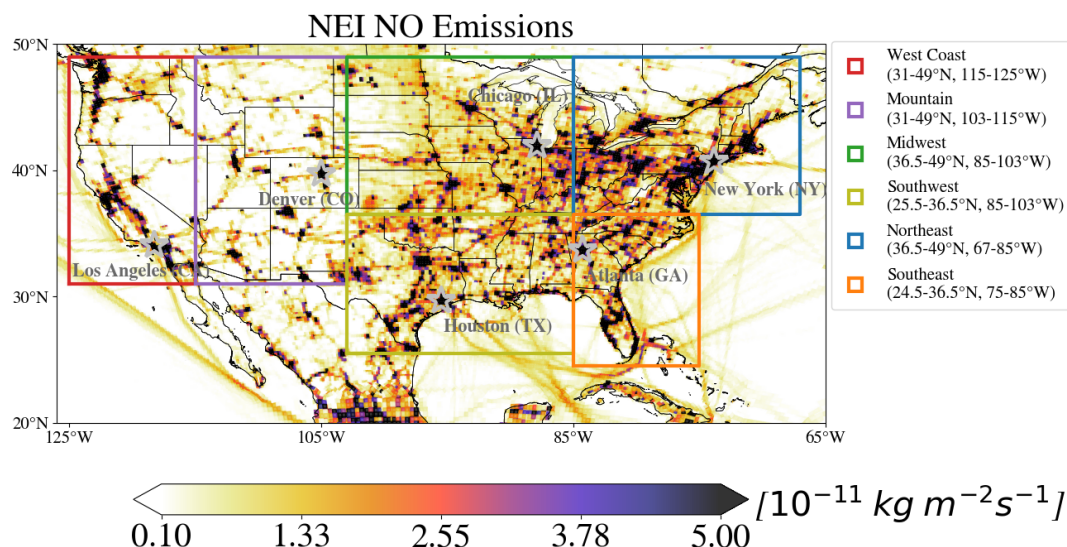


**Figure 1.** July mean nitric oxide (NO) emissions from the 2017 National Emissions Inventory (NEI) adjusted to 2018, divided into six regions for model analysis: West Coast (red), Mountain (purple), Midwest (green), Southwest (yellow), Northeast (blue), and Southeast (orange). The locations of selected State and Local Monitoring Stations (SLAMS) in six major cities – Los Angeles (CA), Denver (CO), Chicago (IL), Houston (TX), New York City (NY), and Atlanta (GA) – are marked with stars.

$4 \times 10^{15} \text{ molec. cm}^{-2}$ ) across the six regions. CO  $\text{VCD}_{\text{Total}}$  is underestimated by 2%–11% ( $3\text{--}18 \times 10^{16} \text{ molec. cm}^{-2}$ ) in the West Coast, Midwest, and Northeast, but overestimated by 2%–8% ( $3\text{--}14 \times 10^{16} \text{ molec. cm}^{-2}$ ) in the Mountain, Southwest, and Southeast regions.

Compared to the *BASE* case, *NEI\_monthly* (Table 1) improves spatial correlations ( $r_s$ ) and reduces model biases (MBE and RMSE) for surface NO<sub>2</sub>, CO, and O<sub>3</sub> concentrations, particularly in the Northeast (Fig. 2a; Table S2). Differences in simulated surface NO<sub>2</sub> and CO between *NEI\_monthly* and *BASE* (Fig. 3a) reflect emissions changes in NO and CO due to the shift from CAMS-GLOB-ANT v5.1 to NEI (Fig. S4). Lower NEI NO emissions (Fig. S4c) reduce regional mean NO<sub>2</sub> concentrations by 1–6 ppb, bringing high biases down to within 1 ppb but exacerbating the low bias in the Mountain region to –2 ppb (Fig. 2a). CO concentrations increase relative to the *BASE* simulation (Fig. 3a), improving the surface CO underestimation by 13%–55% (20–65 ppb), although low biases of 1%–33% (2–71 ppb) remain (Fig. 2a). For secondary pollutants like O<sub>3</sub>, changes in concentrations do not directly mirror emissions perturbations. Surface O<sub>3</sub> concentrations decrease in *NEI\_monthly* relative to *BASE*, reducing modeled surface O<sub>3</sub> biases relative to SLAMS by 2%–11% (approximately 1–6 ppb) on average across the six regions (Figs. 2a and 3a). However, model biases of 3%–21% (1–8 ppb) remain across all regions, particularly on the West Coast (*NEI\_monthly* in Fig. 2a).

There are minimal to no changes in  $r_s$  for HCHO  $\text{VCD}_{\text{Trop}}$ , while NO<sub>2</sub>  $\text{VCD}_{\text{Trop}}$  shows weaker correlations and worsening model biases (Fig. 2b; Table S2). Changes in CO  $\text{VCD}_{\text{Total}}$  exhibit large regional variability (Fig. 3b). Switch-

ing to NEI consistently decreases both surface and column NO<sub>2</sub> but not CO (Fig. 3). Compared to *BASE*, *NEI\_monthly* worsens the model underestimates of NO<sub>2</sub>  $\text{VCD}_{\text{Trop}}$  by 16%–21% ( $\sim 1 \times 10^{14} \text{ molec. cm}^{-2}$ ) but decreases overestimates of regional mean HCHO  $\text{VCD}_{\text{Trop}}$  by approximately 2% ( $0.2\text{--}4 \times 10^{14} \text{ molec. cm}^{-2}$ ) across all regions (Fig. 2b). CO  $\text{VCD}_{\text{Total}}$  changes little (Fig. 3b), with the sign of the model bias unchanged from *BASE* (Fig. 2b).

Biases in trace gas columns do not always match those at the surface. For instance, surface NO<sub>2</sub> is biased high in some regions especially in *BASE*, while NO<sub>2</sub>  $\text{VCD}_{\text{Trop}}$  are consistently biased low relative to TROPOMI (Fig. 2). These different biases in the surface versus column can arise from several factors that are independent of surface emission magnitude, including: (i) vertical sensitivity and representativeness, given that satellite columns reflect vertically weighted pixel means whereas surface observations are point measurements; and (ii) retrieval uncertainties, including assumptions in the air mass factor calculation and the stratosphere-troposphere separation applied to derive tropospheric NO<sub>2</sub> columns (van Geffen et al., 2020). In addition, prior global chemistry models have been shown to underestimate background NO<sub>2</sub>  $\text{VCD}_{\text{Trop}}$  relative to satellite products, partly due to uncertainties in free-tropospheric NO<sub>x</sub> chemistry (e.g., NO/NO<sub>2</sub> ratios and partitioning among reactive nitrogen species) (van Geffen et al., 2022; Shah et al., 2023; Silvern et al., 2018, 2019).

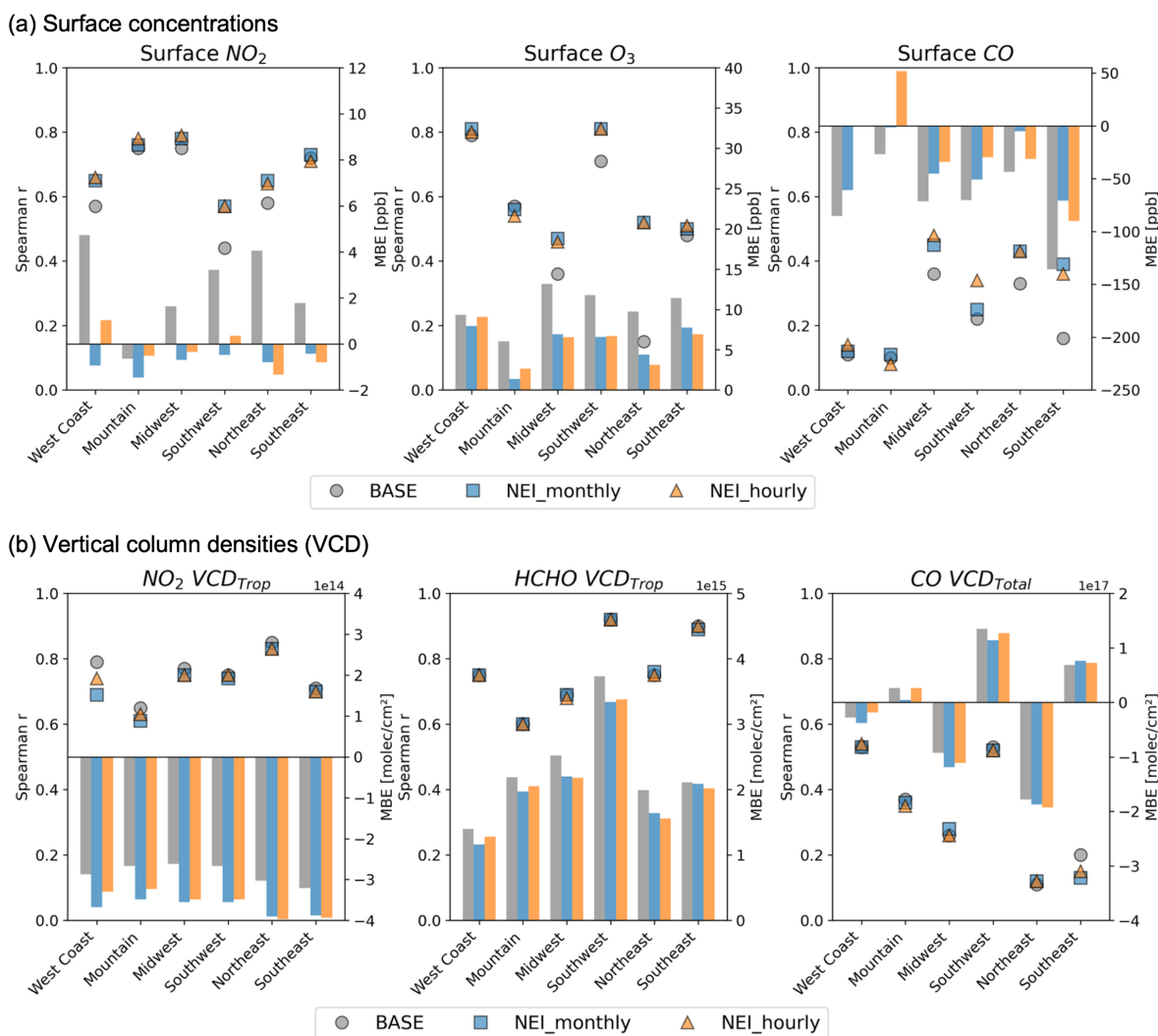


**Figure 2.** Switching to monthly NEI emissions generally improves spatial correlations and reduces biases compared with observations, whereas changes in the temporal resolution of emissions have smaller effects but regionally these impacts differ. Shown are MUSICAv0-simulated (a) surface concentrations of NO<sub>2</sub>, O<sub>3</sub>, and CO, and (b) column densities of tropospheric NO<sub>2</sub>, tropospheric HCHO, and total CO compared with observations (AQS for surface; TROPOMI for columns) for July 2018 across the six U.S. regions indicated in Fig. 1. Mean bias error (MBE; right axis) is shown as colored bars, and Spearman correlation coefficients ( $r_s$ ; left axis) are shown as colored markers with distinct shapes. Colors indicate different model simulations (Table 1): *BASE* (gray bars/circles), *NEI<sub>monthly</sub>* (blue bars/squares), and *NEI<sub>hourly</sub>* (orange bars/triangles). See Table S2 for detailed statistics, including both the absolute and relative differences in MBE and root mean square error (RMSE).

### 3.3 Incorporating Hourly Variations in Emissions (*NEI<sub>hourly</sub>*) Affects Monthly Mean Pollutant Concentrations

The surface NO<sub>2</sub> and O<sub>3</sub> concentration changes between *NEI<sub>hourly</sub>* and *NEI<sub>monthly</sub>* are, in some regions, similar in magnitude to those between *NEI<sub>monthly\_m30anthroNO</sub>* (a 30% reduction in anthropogenic NO emissions) and *NEI<sub>monthly</sub>*, but the spatial patterns differ markedly (Fig. 3a), reflecting the temporal redistribution of emissions. Although the overall agreement with observations changes only slightly ( $r_s$ , MBE, and RMSE; Fig. 2 and Tables S2 and

S3), the direction and magnitude of concentration changes vary across regions, especially between urban and rural areas and between the western and eastern CONUS (Figs. 3 and 4).

The largest July regional-mean difference in surface NO<sub>2</sub> concentrations (*NEI<sub>hourly</sub>* – *NEI<sub>monthly</sub>*) occurs on the West Coast (+16%, or +0.3 ppb), while NO<sub>2</sub> decreases most in the Northeast (–7%, –0.1 ppb) (Fig. 3a). As a result, the model shifts from underestimation to overestimation on the West Coast, while the underestimation in the Northeast is exacerbated versus the surface NO<sub>2</sub> SLAMS observations

(Fig. 2a). Changes in surface CO are small and spatially varied, with regional mean increases of 2 %–7 % (4–10 ppb) in the West Coast, Mountain, Midwest, and Southwest, and decreases of about 3 % (~ 5 ppb) in the Northeast and Southeast (Fig. 3a). Changes in NO<sub>2</sub> VCD<sub>Trop</sub> and CO VCD<sub>Total</sub> largely mirror the surface patterns (Fig. 3b).

High model biases persist for surface O<sub>3</sub> concentrations (5 %–20 %; 3–9 ppb) after incorporating hourly variations in emissions (*NEI\_hourly* in Fig. 2a). Monthly mean surface O<sub>3</sub> concentrations decrease by up to ~ 2 % (< 1 ppb) in the Midwest, Northeast, and Southeast, while increases of up to ~ 3 % (1–4 ppb) in other regions slightly worsen model overestimation. Previous studies also find model overestimates of near-surface O<sub>3</sub>, with the most significant biases in the Southeast U.S., possibly reflecting uncertainties in isoprene–NO<sub>x</sub>–O<sub>3</sub> chemistry, inaccuracies in dry deposition and forest canopy parameterization, and overestimates in NO<sub>x</sub> emissions (Baublitz et al., 2020; Fiore et al., 2009; Makar et al., 2017; Martin et al., 2014; Schwantes et al., 2020; Travis et al., 2016). Although surface HCHO observations are unavailable for evaluation, modeled changes remain under 3 % and follow similar spatial patterns to those of surface O<sub>3</sub> (Fig. 3a). Monthly mean HCHO VCD<sub>Trop</sub> decreases in the Midwest, Northeast, and Southeast but increases in other regions, mirroring the regional pattern of surface HCHO changes (Fig. 3), though a general high model bias of 14 %–23 % ( $1\text{--}3 \times 10^{15}$  molec. cm<sup>-2</sup>) persists (Fig. 2b; Table S2).

### 3.4 Model Evaluation: Diurnal Variability and Weekday-Weekend Differences

Our model simulations (Table 1) broadly capture day-to-day variations in surface NO<sub>2</sub> and O<sub>3</sub> at the six urban sites (Fig. S10), but they tend to overestimate both the daily range and the weekday-weekend differences and misrepresent the timing of peak concentrations in most cities (Fig. S11). The exaggerated daily range reflects opposite model biases at different times of day: the model overestimates nighttime NO<sub>2</sub> (when concentrations are highest) and fails to capture the nighttime minimum in O<sub>3</sub>, while at midday it underestimates NO<sub>2</sub> and overestimates O<sub>3</sub> (Fig. S11). As expected, simulations with day-to-day variations in emissions better capture weekday-weekend concentration differences compared to *NEI\_monthly*, though the diurnal shape still does not fully capture observations (see the right column of Fig. S11). The model also misrepresents the timing of daily peaks. For example, the simulated NO<sub>2</sub> maximum occurs at 06:00 a.m. in Los Angeles, about two hours earlier than observed (Fig. S11).

It is challenging for models to accurately represent the complex diurnal processes that shape near-surface concentrations, including boundary-layer evolution (Adams et al., 2023). Our MUSICAv0 simulations use the standard CAM6 planetary boundary layer parameterization, the Cloud Layers Unified By Binormals (CLUBB) (Bogenschütz et al.,

2018; Danabasoglu et al., 2020). While prior evaluation within the CESM2/CAM6 framework shows that the scheme generally captures the broad diurnal and seasonal structure of boundary-layer behavior, overly strong nocturnal mixing leads to errors in the timing of the morning transition although the specific biases vary across regions and seasons (Holtslag et al., 2013; Schwantes et al., 2022; Stjern et al., 2023). These biases will be reflected in the simulated diurnal amplitude and timing of near-surface concentration peaks and their relationship to the underlying temporal profile of emissions. Errors may also arise from the NEI diurnal profiles applied in this study, which are sector-specific and derived from activity-based temporal allocation methods whose accuracy at local scales is uncertain. In addition, comparisons between model grid-cell means and individual SLAMS sites inevitably involve representativeness differences that may contribute to mismatches.

## 4 Sensitivity to Resolving Hourly Variations in Nitric Oxide Emissions

Imposing hourly-varying emissions results in spatially heterogeneous changes even in the monthly mean surface NO<sub>2</sub>, O<sub>3</sub>, and HCHO concentrations, with strong west-east and urban-rural contrasts (Figs. 3–5). We demonstrate that these simulated responses produced by switching from *NEI\_monthly* to *NEI\_hourly* are primarily driven by the hourly variations in NO emissions, evidenced by minimal changes between *NEI\_hourly\_NO* and *NEI\_hourly* (< 0.5 % for NO<sub>2</sub>, HCHO, and O<sub>3</sub>). Comparisons between *NEI\_daily\_NO* and *NEI\_monthly*, and between *NEI\_hourly\_NO* and *NEI\_daily\_NO*, indicate that these spatial patterns are shaped by switching from daily mean to hourly varying NO emissions (Figs. 3 and S12). As illustrated in Fig. 6, switching from daily mean to hourly NO emissions increases daytime and decreases nighttime emissions, with larger differences on weekdays, thereby influencing surface NO<sub>x</sub> concentrations and secondary pollutants like O<sub>3</sub>.

### 4.1 West-East Contrasts in Surface Pollutant Responses

To understand the broader impacts of incorporating hourly NO emissions, we begin by examining regional contrasts in July daytime (09:00 a.m.–05:00 p.m. local time) responses across the CONUS, as shown in Fig. 5. Panel a maps the differences in surface NO, NO<sub>2</sub>, O<sub>3</sub>, and HCHO concentrations (*NEI\_hourly\_NO* minus *NEI\_daily\_NO*), while panel b summarizes the meridional means in 5° longitudinal bins. These plots highlight a west-to-east gradient in pollutant responses driven solely by adding the diel cycle to NO emissions. To help interpret this spatial variability, panel c presents the corresponding *NEI\_daily\_NO* daytime emissions and key meteorological variables, including surface temperature, planetary boundary layer height (PBLH;

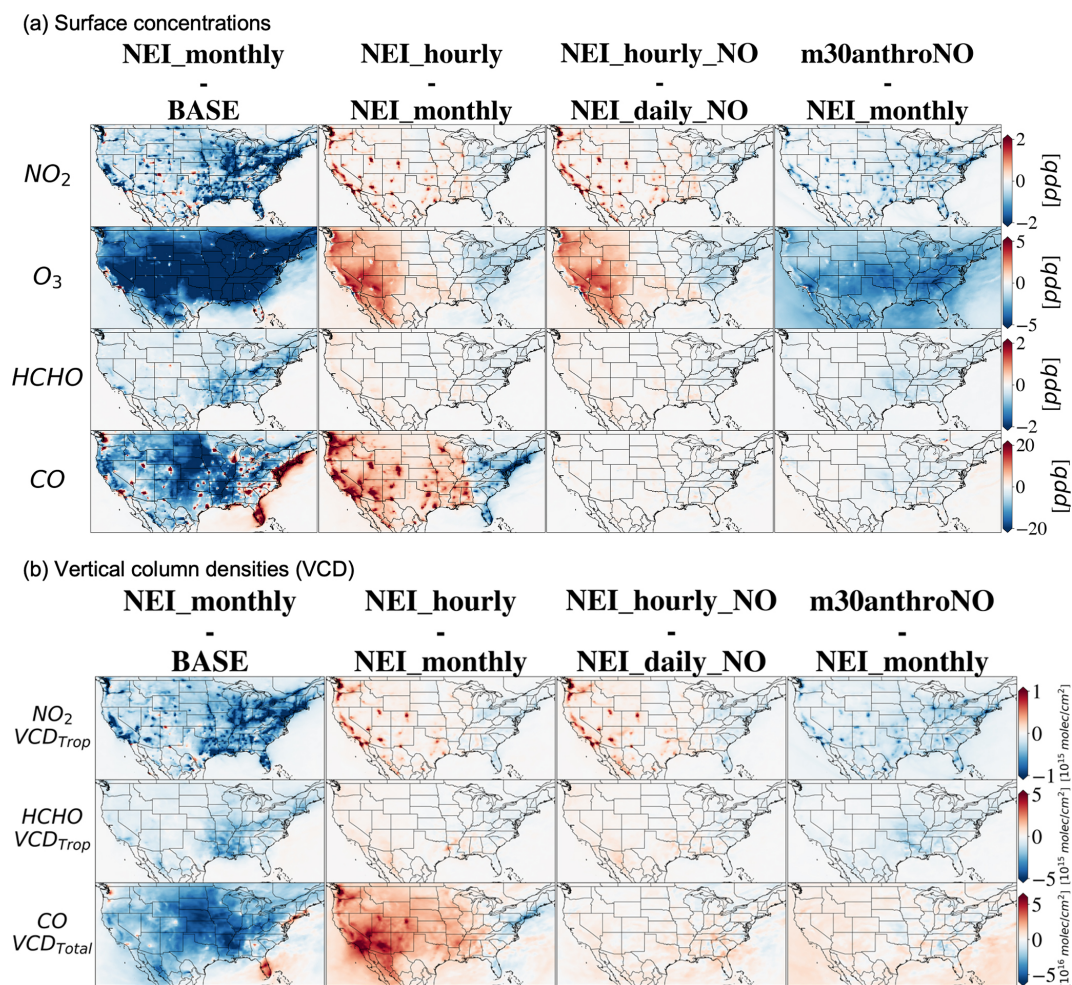


**Figure 3.** Changes produced by switching from *BASE* to *NEI\_monthly* (left column), and by resolving hourly variations in NO emissions produces distinct spatial responses in July monthly mean (middle two columns; see Table 1): (a) surface concentrations, with absolute changes comparable to those from a uniform 30 % reduction in monthly mean NO emissions (right column); and (b) column densities, which generally mirror surface responses. Consistent color-bar ranges are used for each variable. See Fig. S2b for differences in surface SO<sub>2</sub> and PM<sub>2.5</sub>.

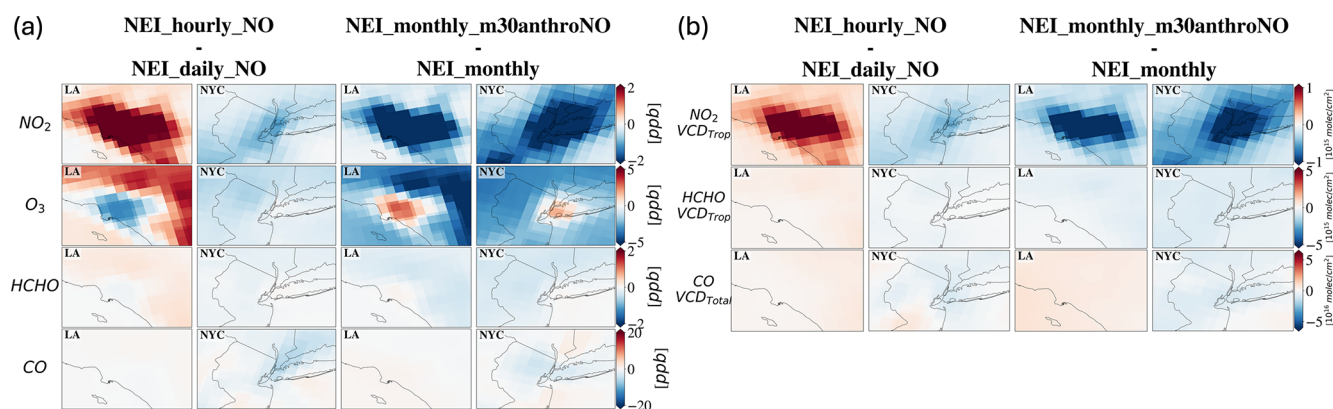


**Figure 4.** Changes produced over Los Angeles (LA) and New York City (NYC) by resolving hourly NO emissions (first two columns) versus a uniform 30 % decrease in anthropogenic NO emissions (two right-most columns) for (a) surface concentrations and (b) column densities.

m a.g.l.), relative humidity, and NO<sub>2</sub> lifetime against dry deposition.

Polluted urban regions with higher NO emissions (Fig. 1) show more pronounced NO<sub>x</sub> concentration responses (Figs. 3 and 4). In the western CONUS, July daytime (09:00 a.m.–05:00 p.m.) monthly mean surface NO and NO<sub>2</sub> concentrations increase by up to 8 and 6 ppb, respectively, in urban areas in *NEI\_hourly\_NO* simulation relative to *NEI\_daily\_NO* (Fig. 5a–b). In contrast, monthly mean daytime surface NO and NO<sub>2</sub> decrease over the eastern CONUS by up to ~1 ppb, respectively, with the largest changes also concentrated in urban areas. However, changes in surface O<sub>3</sub> do not always coincide with the largest NO<sub>x</sub> concentration changes. In the eastern CONUS, O<sub>3</sub> decreases by up to ~2 ppb (Fig. 5a–b), with the largest reductions over the polluted urban centers, consistent with prior findings (e.g., Jo et al., 2023). In contrast, monthly mean O<sub>3</sub> increases of up to 8 ppb occur over the western CONUS along the edges of urban areas (Fig. 5a). This spatial pattern points to enhanced NO<sub>x</sub> sensitivity at the periphery of NO<sub>x</sub>-saturated western urban cores; similar patterns occur in the *NEI\_monthly\_m30anthroNO* sensitivity simulation relative to the *BASE* case, where the 30% reduction in anthropogenic NO emissions yields the largest O<sub>3</sub> changes in surrounding rural areas (Figs. 3 and 4). In the West, the mean of the *NEI\_hourly\_NO* minus *NEI\_daily\_NO* differences exceeds the median (Fig. 5b), driven by large NO<sub>x</sub> increases in a few urban grid cells. In the East, the larger mean decreases relative to the median similarly reflect strong but localized NO<sub>x</sub> decreases. By contrast, O<sub>3</sub> differences show closer agreement between mean and median across both regions, suggesting more spatially uniform impacts (Fig. 5c).

These spatial patterns are shaped by a complex interplay of background anthropogenic and biogenic emissions, local photochemical conditions, meteorology (especially boundary layer dynamics and transport), and deposition. In July, the East Coast has higher background NO emissions, approximately 70% higher over the Northeast region than over the West Coast (Fig. 1). In the western U.S., anthropogenic emissions tend to occur in more localized hotspots in contrast to the continuous, corridor-like pattern in the eastern U.S., consistent with population density and urban clustering (Fig. S4a). Biogenic emissions, dominated by isoprene and monoterpenes, are highest and widespread across the eastern and southern CONUS (Fig. S5). Switching to hourly emissions generally increases daytime NO (Fig. 6), yet the resulting impact on surface concentrations across the CONUS (Fig. 5a) differs notably from the response to a uniform 30% reduction in anthropogenic NO emissions (Fig. 3). This finding indicates that the timing of anthropogenic emissions perturbations with respect to other processes like meteorology (Fig. 5c), biogenic emissions, and deposition shape the contrasting changes between the western and eastern CONUS. For example, shallower daytime PBLH such as over the eastern CONUS can limit vertical mixing while enhancing both

photochemical reactions and surface deposition (Wu et al., 2024). Together with higher humidity, these processes may contribute to a shorter NO<sub>2</sub> lifetime in the eastern CONUS during July 2018. We explored the possibility of a persistent synoptic-scale east-west dipole in air stagnation, defined according to the meteorological criteria of Wang and Angell (1999), but did not find any evidence for such a feature.

#### 4.2 Urban Case Studies: Los Angeles vs. New York City

To further investigate the regional contrasts introduced in Sect. 4.1, we examine two representative urban centers, Los Angeles (CA) and New York City (NY), to show how local-scale meteorology and photochemistry interact with hourly NO emission patterns to produce opposite-signed responses in NO<sub>x</sub> and O<sub>3</sub> concentrations. Figure 6 compares *NEI\_hourly\_NO* and *NEI\_daily\_NO* simulations, showing (a) time series of NO emissions and surface NO concentration differences, (b) July weekday-averaged diel differences in NO, NO<sub>2</sub>, O<sub>3</sub>, and HCHO, and (c) weekday-averaged diel cycles of NO emissions, surface NO, and PBLH. Weekend patterns are similar but generally smaller in magnitude (see Fig. S13). Figure 7 presents July daytime O<sub>3</sub> production rates ( $P(O_3)$ , diagnosed in MUSICAv0 as chemical O<sub>3</sub> production from reactions of NO with the hydroperoxy radical and organic peroxy radicals) binned by surface NO<sub>x</sub> concentrations for the *NEI\_monthly*, *NEI\_hourly\_NO*, and *NEI\_monthly\_m30anthroNO* simulations. Box plots summarize the distribution of  $P(O_3)$  within uneven NO<sub>x</sub> concentration bins (e.g., 0–1, 1–2, ..., 5–10, 10–15, ..., > 50 ppb); color-coded points highlight values during morning, noon, and afternoon periods. Figures S7, S13 and S14 include our findings for all major cities shown in Fig. 1.

Comparing *NEI\_hourly\_NO* to *NEI\_daily\_NO*, surface NO<sub>x</sub> concentrations decrease in New York City but increase in Los Angeles, especially during the morning rush hour when the boundary layer is growing (Fig. 6b–c). Monthly mean surface O<sub>3</sub>, however, decreases in both Los Angeles and New York City, though the magnitudes differ (Fig. 4a). Surface O<sub>3</sub> decreases most in Los Angeles on weekdays between 09:00 a.m. and 03:00 p.m., outweighing a smaller late-afternoon increase (03:00–06:00 p.m.) (Fig. 6b). In New York City, the net monthly mean decrease is minimal because modest reductions from noon to evening (12:00–06:00 p.m.) only slightly exceed the morning increase (08:00 a.m.–12:00 p.m.) (Fig. 6b).

To assess the sensitivity of  $P(O_3)$  to NO<sub>x</sub> and VOC, we compare  $P(O_3)$  in *NEI\_monthly\_m30anthroNO* and *NEI\_monthly\_m30anthroVOC* with *NEI\_monthly* (Table 1). All three simulations indicate that New York City and Los Angeles are generally NO<sub>x</sub>-saturated, with surface O<sub>3</sub> increasing as NO emissions decrease (Fig. 4a) and little change in response to the 30% reduction in anthropogenic VOC emissions (< 0.5% across all regions; not shown). Previous studies have shown that O<sub>3</sub> production

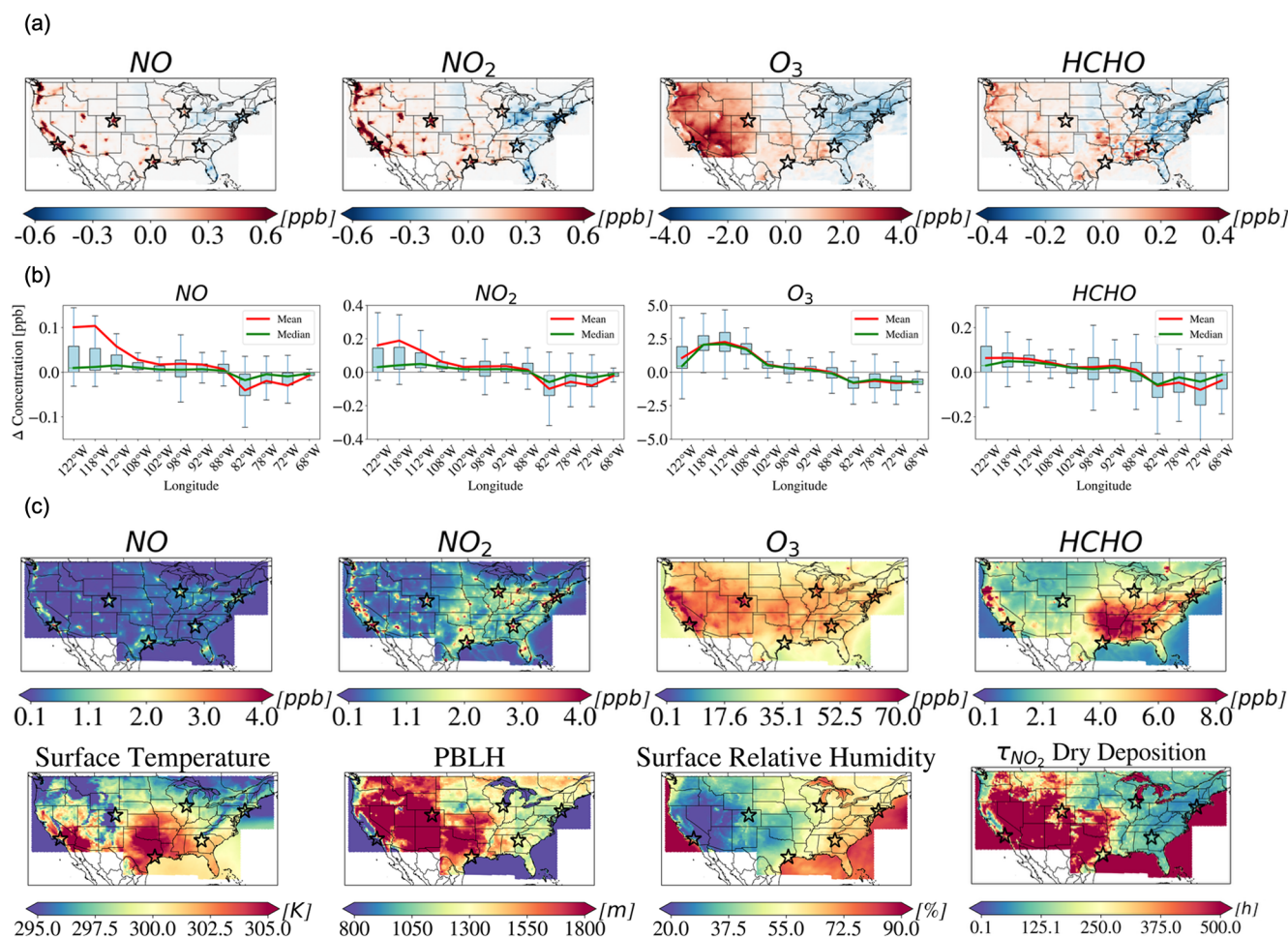


**Figure 5.** Resolving hourly NO emissions results in contrasting surface responses between the western and eastern CONUS and between urban and rural areas. Panel (a) shows monthly mean July daytime (09:00 a.m.–05:00 p.m. local time) differences in simulated surface concentrations of NO, NO<sub>2</sub>, O<sub>3</sub>, and HCHO (*NEI\_hourly\_NO* minus *NEI\_daily\_NO*). Panel (b) provides a meridional summary of the July daytime differences shown in panel (a), with values averaged within 5° longitude bins across CONUS latitudes (23–50° N). Each boxplot shows the interquartile range (25th–75th percentiles) within each longitude bin, with whiskers extending to 1.5 × interquartile range (outliers excluded); red and green lines denote the mean and median, respectively. The horizontal line marks zero change. Panel (c) displays monthly mean July daytime values from the *NEI\_daily\_NO* simulation. The first row presents surface concentrations of NO, NO<sub>2</sub>, O<sub>3</sub>, and HCHO, and the second row includes relevant meteorological variables: surface temperature, planetary boundary layer height (PBLH; m a.g.l.), and surface relative humidity. The rightmost plot in the second row shows the surface NO<sub>2</sub> lifetime against dry deposition loss.

tends to become more NO<sub>x</sub>-sensitive around noon and in the afternoon, when photochemical conditions are most favorable for O<sub>3</sub> formation (Tao et al., 2022). In contrast, the model indicates a *P*(O<sub>3</sub>) peak during the late morning in both New York City and Los Angeles, particularly in *NEI\_monthly\_m30anthroNO* (Fig. 7c, f). Compared to *NEI\_monthly* (Fig. 7a, d), *NEI\_monthly\_m30anthroNO* (Fig. 7c, f) shifts the NO<sub>x</sub> concentration bins associated with high *P*(O<sub>3</sub>) toward lower NO<sub>x</sub> in both Los Angeles and New York City. For example, in Los Angeles, the highest-NO<sub>x</sub> conditions (> 30 ppb) shift into lower NO<sub>x</sub> bins (< 30 ppb) (Fig. 7a, c).

Incorporating hourly NO emissions (*NEI\_hourly\_NO*) reduces July mean daytime *P*(O<sub>3</sub>) relative to *NEI\_monthly* by ~ 2 ppb h<sup>-1</sup> in Los Angeles and ~ 0.3 ppb h<sup>-1</sup> in New York City. Using hourly NO emissions (*NEI\_hourly\_NO*) increases the density of values in the highest NO<sub>x</sub> bins in Los Angeles while maintaining similar *P*(O<sub>3</sub>) values in those bins (Fig. 7b), extending the high-NO<sub>x</sub> tail of the *P*(O<sub>3</sub>)-NO<sub>x</sub> distribution into more strongly NO<sub>x</sub>-saturated conditions (compare Fig. 7a vs. Fig. 7b). This enhanced high-NO<sub>x</sub> tail reflects larger morning NO<sub>x</sub> concentrations, when the chemical regime is most NO<sub>x</sub>-saturated and O<sub>3</sub> production is suppressed. Although conditions become more NO<sub>x</sub>-sensitive later in the afternoon (Fig. 7b), the larger O<sub>3</sub>

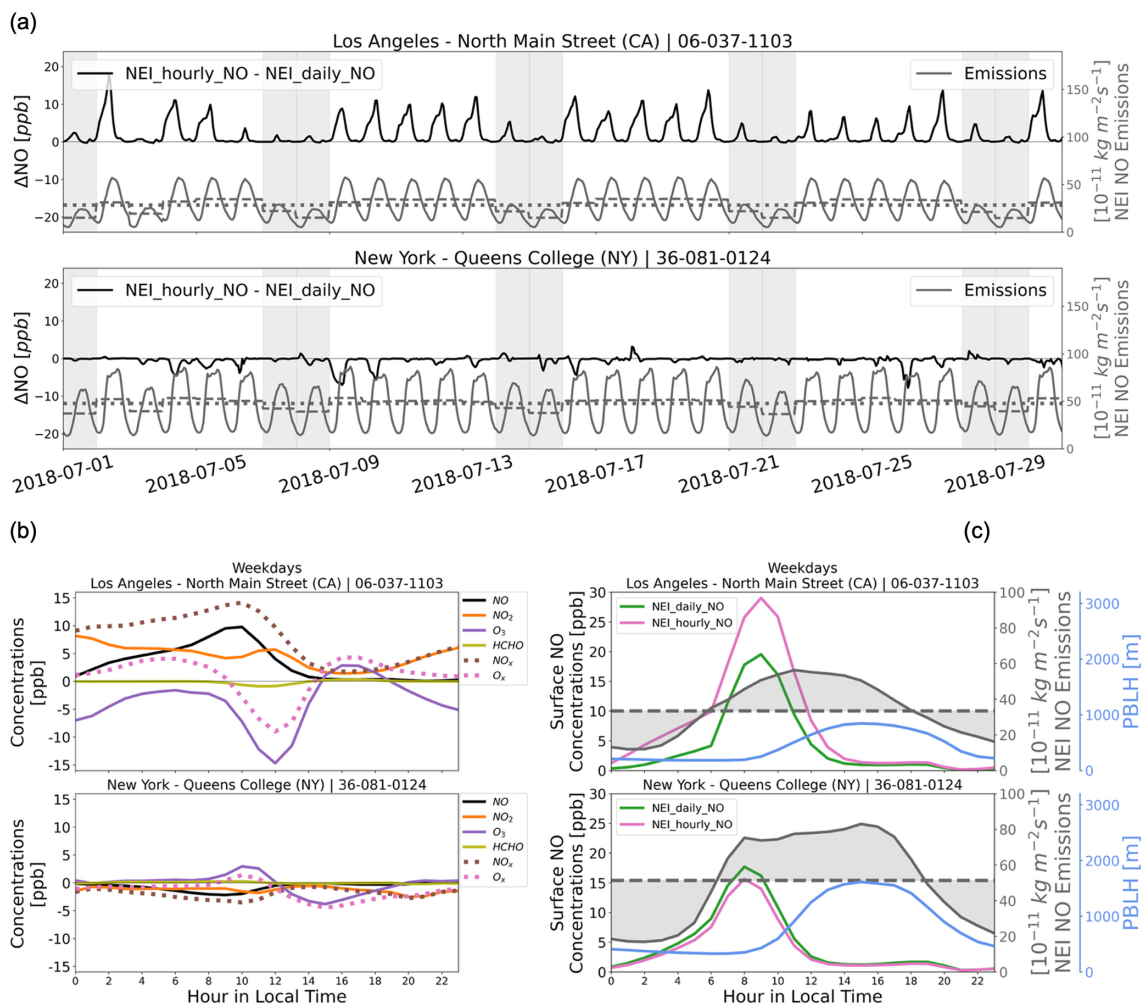


**Figure 6.** Despite similar diurnal variation in NO emissions – higher during daytime, lower at night – Los Angeles and New York City show different pollutant responses reflecting city-specific emission timing, boundary layer dynamics, and local photochemistry. **(a)** Hourly time series of July differences in surface NO concentrations between *NEI\_hourly\_NO* and *NEI\_daily\_NO* (black solid lines), alongside hourly (solid gray), daily mean (dashed), and monthly mean (dotted) NO emissions. Weekend days are shaded in gray. The lower-than-typical weekday emissions on 3 July 2018 reflect the July 4th holiday pattern in the 2017 NEI data following the shift to the 2018 calendar. Also shown are July 2018 weekday average **(b)** hourly surface concentration differences between *NEI\_hourly\_NO* and *NEI\_daily\_NO* for NO (black), NO<sub>2</sub> (orange), O<sub>3</sub> (purple), and HCHO (olive green), with NO<sub>x</sub> (≡ NO + NO<sub>2</sub>; brown) and O<sub>x</sub> (≡ O<sub>3</sub> + NO<sub>2</sub>; pink) shown as dotted lines; **(c)** hourly NO concentrations from *NEI\_daily\_NO* (green) and *NEI\_hourly\_NO* (pink), NO emissions (gray) and PBLH (blue) for Los Angeles (top) and New York City (bottom). Solid lines represent the mean weekday diel cycle of emissions, while dashed lines show the corresponding weekday mean across all hours. Weekend days show similar patterns but with smaller magnitudes of change (Fig. S13). Results for all sites (including Chicago, Denver, Houston, and Atlanta; see Fig. 1), with both weekday and weekend averages shown for panels **(b)**–**(c)**, are provided in Fig. S13.

decrease during late morning to early afternoon (~ 09:00–14:00 LT; Fig. 6b) dominates the net monthly mean O<sub>3</sub> concentration response in Los Angeles (Fig. 4a). The more temporally concentrated (peaky) emission profile and shallower daytime PBL heights in Los Angeles compared to New York City (Fig. 6c) likely amplifies NO<sub>x</sub> accumulation, reinforcing a NO<sub>x</sub>-saturated regime. We find that Los Angeles, Denver, and Houston show broadly similar responses to hourly versus monthly mean NO emissions, while New York City,

Chicago, and Atlanta exhibit distinct behavior (Figs. S13 and S14).

#### 4.3 Implications for Satellite-Based NO<sub>x</sub> Emission Constraints

Our results in Sect. 4.1 and 4.2 show that resolving hourly NO emissions changes simulated NO<sub>2</sub> VCD<sub>Trop</sub> even when the total monthly emissions are the same. Given that NO<sub>2</sub> VCD<sub>Trop</sub> observations from satellites are commonly used to

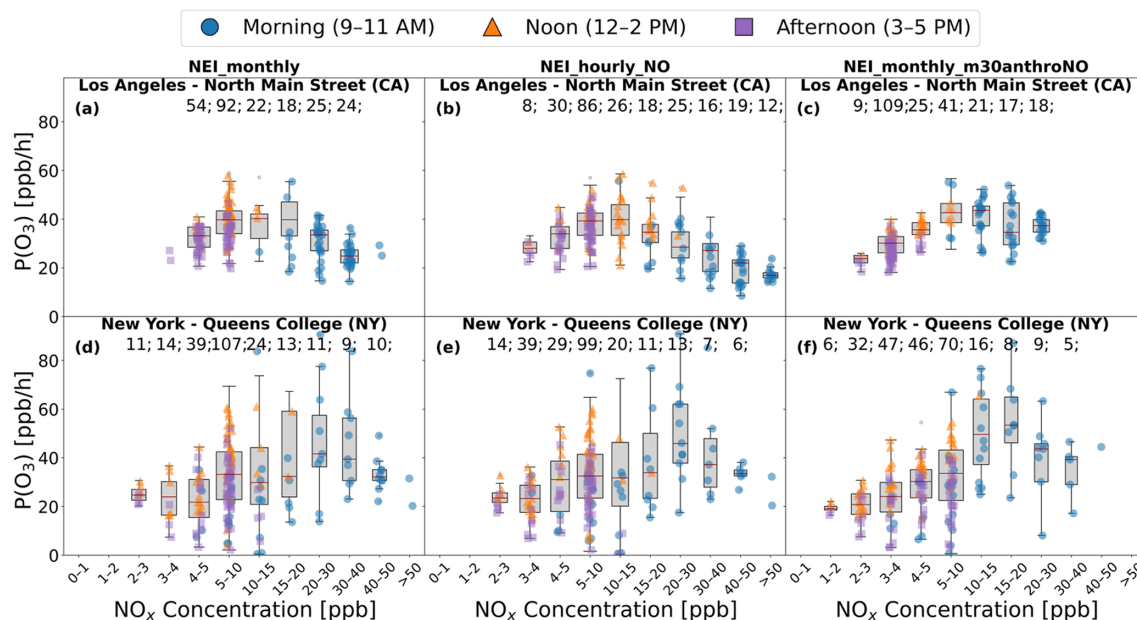


**Figure 7.** Modeled hourly  $P(\text{O}_3)$  ( $\text{ppb h}^{-1}$ ) versus surface  $\text{NO}_x$  concentrations (ppb) for July daytime hours (09:00 a.m.–05:00 p.m.) in *NEI\_monthly* (left column), *NEI\_hourly\_NO* (middle), and *NEI\_monthly\_m30anthroNO* (right) sampled at the selected Los Angeles (CA; **a–c**) and New York (NY; **d–f**) monitoring site. Colored points highlight local morning (09:00–11:00 a.m., blue circles), noon (12:00–02:00 p.m., orange triangles), and afternoon (03:00–05:00 p.m., purple squares). Boxplots summarize the distribution of  $P(\text{O}_3)$  within uneven  $\text{NO}_x$  bins (e.g., 0–1, 1–2, ..., 5–10, 10–15, ..., > 50 ppb) plotted at equal spacing along the  $x$  axis. Only bins containing at least five data points are shown, and the sample size is indicated above each corresponding box; box widths are scaled to the sample size. Results for additional sites (Chicago, Denver, Houston, and Atlanta) are included in Fig. S14.

derive top-down constraints on  $\text{NO}_x$  emissions, differences in the timing of emissions in models used for such inversions may alter the inferred emission estimates.  $\text{NO}_x$  emissions are sometimes inferred using proportional scaling or mass-balance approaches, in which *a priori* emissions are adjusted based on the ratio of observed to modeled  $\text{NO}_2$  columns, for example with chemical transport models that implicitly represent the impacts of transport and chemistry along with emissions on atmospheric concentrations (Lamsal et al., 2011, 2014; Martin et al., 2003). More formal inverse modeling and data assimilation frameworks exist but similarly depend on satellite overpass-time  $\text{NO}_2$  columns and model representations of diurnal variability (Goldberg et al., 2019; Miyazaki and Eskes, 2013).

To estimate potential biases in the inferred NO emission magnitude arising from model representation of diurnal emission timing, we perform a simple, one-month scaling-based approach for July 2018 (details in Sect. S6). In this section,  $\Omega$  denotes  $\text{NO}_2$  VCD<sub>Trop</sub> and  $E$  anthropogenic NO emissions. While our illustrative simple framework assumes a local relationship between  $\Omega$  and  $E$ , we emphasize that  $\Omega$  will generally reflect emissions from multiple model grid cells given the  $\text{NO}_x$  lifetime and transport timescales. Transport, chemistry, and lifetime effects are implicitly accounted for through the forward model but are not explicitly inverted. Accordingly,  $(\Delta E/E)_{\text{est}}$  in Fig. 8 should be interpreted as

an estimate of the potential bias in inferred emission magnitude rather than as a quantitative emission inversion. By comparing *NEI\_hourly\_NO* and *NEI\_monthly* to isolate the effect of NO emission timing alone since both simulations use identical monthly-integrated emissions, we find that the inferred timing-representation bias is small on average over the CONUS (+1.8 %) but spatially variable, with regional mean values of 1 %–8 % in the western U.S. and approximately –3 % to –2 % in the Northeast and Southeast (Fig. 8; Table S6). City-scale values are larger, reaching +26 % in Los Angeles, +30 % in Denver and –7 % in New York City (Table S6).

## 5 Discussion and Conclusions

We demonstrated that inclusion of hourly variations in NO emissions in the MUSICAv0 model produces substantial changes in  $\text{NO}_x$  and  $\text{O}_3$  concentrations, even in monthly averages, comparable in magnitude to those associated with an idealized 30 % reduction in NO emissions (Figs. 3 and 4). In contrast to a uniform 30 % reduction in  $\text{NO}_x$ , however, the changes in response to the timing of NO emissions differ between urban and rural areas and between the eastern and western U.S., reflecting region-specific emission patterns, photochemistry, and meteorological conditions (Fig. 5). Monthly mean daytime surface  $\text{O}_3$  concentrations

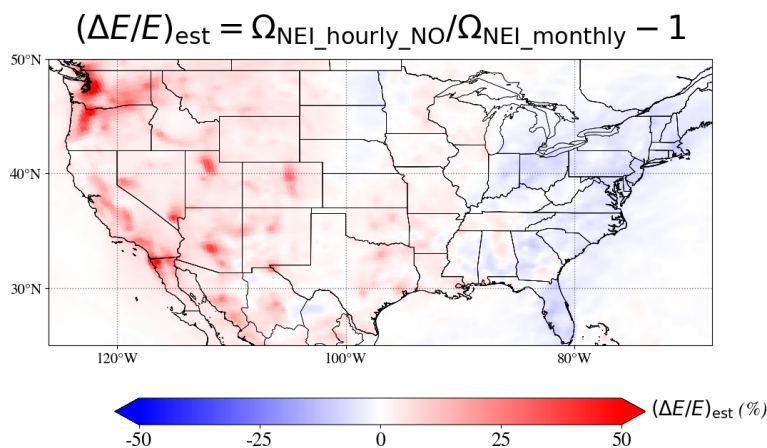


**Figure 8.** Estimated potential relative biases ( $(\Delta E/E)_{\text{est}}$ ; %) in July 2018 anthropogenic NO emissions magnitude ( $E$ ) resulting from neglecting hourly NO emissions, derived by comparing July-mean tropospheric NO<sub>2</sub> columns ( $\Omega$ ) simulated in *NEI\_hourly\_NO* versus *NEI\_monthly*. Regional and city-scale statistics are provided in Table S6; see Sect. S6 for detailed methods.

over the CONUS in July differ by up to 7 ppb (11% for *NEI\_hourly* relative to *NEI\_monthly*; Fig. 5), large enough to affect model-based conclusions regarding regional attainment of the U.S. NAAQS for O<sub>3</sub>. We also find differences in O<sub>3</sub> production regimes across cities: for example, a shift toward more NO<sub>x</sub>-saturated conditions in Los Angeles but toward stronger NO<sub>x</sub> sensitivity in New York City when hourly variations in NO emissions are included (Figs. 6 and 7).

When we impose hourly variations in NO emissions, monthly mean surface NO<sub>2</sub> increases over the western CONUS by up to ~6 ppb during the daytime. In contrast, the eastern CONUS with its higher NO and biogenic VOC emissions, larger dry deposition flux rates, more humid conditions, and shallower PBLH – all of which favor a shorter NO<sub>2</sub> lifetime – experiences daytime NO<sub>2</sub> decreases of up to ~1 ppb (Fig. 5). Spatial changes in simulated VCD closely follow those in surface concentrations (Figs. 3 and 4). Using a simple scaling-based analysis, we show that resolving hourly emissions, even with identical monthly total NO emissions, has the potential to alter NO emission magnitudes inferred from monthly-averaged satellite-retrieved NO<sub>2</sub> VCD<sub>Trop</sub> combined with model column-to-surface relationships. For July 2018, we show that neglecting hourly variability in anthropogenic NO emissions leads to spatially heterogeneous biases in the estimated emissions that are generally modest at the regional scale (a few percent) but substantially larger at the grid-cell level, with absolute relative differences ranging from ~1% to > 50% and locally reaching approximately –12% to +56% (Fig. 8).

Since August of 2023, the TEMPO instrument aboard a geostationary satellite is now providing continuous daytime measurements of trace gases over North America (Naeger et al., 2021; Zoogman et al., 2017). Similar geostationary retrievals have been available over East Asia since 2020 from the Geostationary Environment Monitoring Spectrom-

eter (GEMS), with recent studies demonstrating its capability to capture diurnal variations in NO<sub>2</sub> VCD<sub>Trop</sub> (Edwards et al., 2024; Park et al., 2025; Yang et al., 2024). Our results show that neglecting hourly variations in emissions introduces biases when interpreting monthly mean concentrations from once-daily polar-orbiting satellite overpasses, potentially aliasing sub-daily emission variability into top-down NO<sub>x</sub> emission estimates. Emerging geostationary observations now make it possible to evaluate these intra-day effects directly to refine constraints on emission timing as well as related photochemical processes.

Although our analysis focuses on July 2018, the differences we identify due to the temporal resolution of emissions are broadly relevant, though their local magnitude will vary across years with both emissions and meteorology. Recent trends since 2018 could modulate the magnitude of these effects, including: the continued decline in anthropogenic NO<sub>x</sub> emissions (Christiansen et al., 2024); increases in temperature-sensitive soil NO<sub>x</sub> and biogenic VOCs (Geddes et al., 2022); more frequent heat waves and stagnation events (Gao et al., 2023); and episodic wildfires (Abatzoglou et al., 2025). Lower NO<sub>x</sub> emissions and flatter diurnal shapes would likely reduce the differences between using hourly and daily or monthly mean emissions, whereas more stagnant conditions could amplify the O<sub>3</sub> sensitivity to the timing of precursor emissions through enhanced localized photochemistry and deposition. While we analyzed diurnal emission cycles within the CONUS during summer, similar sensitivities are likely to occur in source regions elsewhere, underscoring the need to better characterize diurnal emission cycles and the corresponding chemical responses of air pollutants in other seasons and world regions.

**Code and data availability.** The Multi-Scale Infrastructure for Chemistry and Aerosols version 0 (MUSICAv0) is a pub-

licly available community model maintained by the National Center for Atmospheric Research (NCAR). Source code and documentation can be accessed at: <https://www2.aocom.ucar.edu/sections/MUSICA> (last access: 1 June 2023). Simulation output used in this study has been archived and is available from the corresponding author upon request. Measurements from the State and Local Air Monitoring Stations (SLAMS) network are archived and publicly available through the U.S. Environmental Protection Agency (EPA) Air Quality System Pre-Generated Data Files ([https://aq5.epa.gov/aq5web/airdata/download\\_files.html](https://aq5.epa.gov/aq5web/airdata/download_files.html), U.S. Environmental Protection Agency, 2023). TROPospheric Monitoring Instrument (TROPOMI) Level-2 products are available from the NASA Goddard Earth Sciences Data and Information Services Center (GES DISC) for formaldehyde (<https://doi.org/10.5270/S5P-tjlxfd2>, Copernicus Sentinel-5P, 2018a), nitrogen dioxide (<https://doi.org/10.5270/S5P-s4ljg54>, Copernicus Sentinel-5P, 2018b), and carbon monoxide (<https://doi.org/10.5270/S5P-bj3nry0>, Copernicus Sentinel-5P, 2021).

**Supplement.** The supplement related to this article is available online at <https://doi.org/10.5194/acp-26-6683-2026-supplement>.

**Author contributions.** MT set up the model simulations, performed the data analysis, and wrote the manuscript. AMF provided guidance on scientific direction and simulation design, advised throughout the project, and contributed to manuscript revisions. LKE advised on the use of the MUSICA<sub>v0</sub> model and provided technical guidance. JRS supported the CESM simulations on high-performance computing (HPC) systems. GGP processed the NEI emissions. DSJ advised on preparing emissions for the variable-resolution grid. All co-authors provided comments and suggestions to improve the manuscript.

**Competing interests.** The contact author has declared that none of the authors has any competing interests.

**Disclaimer.** Publisher's note: Copernicus Publications remains neutral with regard to jurisdictional claims made in the text, published maps, institutional affiliations, or any other geographical representation in this paper. The authors bear the ultimate responsibility for providing appropriate place names. Views expressed in the text are those of the authors and do not necessarily reflect the views of the publisher.

**Acknowledgements.** We thank Dr. Joshua Laughner and an anonymous reviewer for their thoughtful and constructive reviews.

**Financial support.** This research has been supported by the National Aeronautics and Space Administration (NASA, Health and Air Quality Applied Sciences Team, HAQAST; grant no. 80NSSC21K0509) and the National Science Foundation (NSF,

grant no. 2228379). The computations presented here were conducted using the “Svante” cluster, a facility located at MIT's Massachusetts Green High Performance Computing Center and supported by the Center for Sustainability Science and Strategy. This work was also supported by the NSF National Center for Atmospheric Research, which is a major facility sponsored by the U.S. National Science Foundation under Cooperative Agreement no. 1852977.

**Review statement.** This paper was edited by Benjamin A Nault and reviewed by Josh Laughner and two anonymous referees.

## References

- Abatzoglou, J. T., Kolden, C. A., Cullen, A. C., Sadegh, M., Williams, E. L., Turco, M., and Jones, M. W.: Climate Change Has Increased the Odds of Extreme Regional Forest Fire Years Globally, *Nat. Commun.*, 16, 6390, <https://doi.org/10.1038/s41467-025-61608-1>, 2025.
- Adams, T. J., Geddes, J. A., and Lind, E. S.: New Insights Into the Role of Atmospheric Transport and Mixing on Column and Surface Concentrations of NO<sub>2</sub> at a Coastal Urban Site, *J. Geophys. Res.-Atmos.*, 128, e2022JD038237, <https://doi.org/10.1029/2022JD038237>, 2023.
- Baublitz, C. B., Fiore, A. M., Clifton, O. E., Mao, J., Li, J., Correa, G., Westervelt, D. M., Horowitz, L. W., Paulot, F., and Williams, A. P.: Sensitivity of Tropospheric Ozone Over the Southeast USA to Dry Deposition, *Geophys. Res. Lett.*, 47, e2020GL087158, <https://doi.org/10.1029/2020GL087158>, 2020.
- Bogenschutz, P. A., Gettelman, A., Hannay, C., Larson, V. E., Neale, R. B., Craig, C., and Chen, C.-C.: The path to CAM6: coupled simulations with CAM5.4 and CAM5.5, *Geosci. Model Dev.*, 11, 235–255, <https://doi.org/10.5194/gmd-11-235-2018>, 2018.
- Christiansen, A., Mickle, L. J., and Hu, L.: Constraining long-term NO<sub>x</sub> emissions over the United States and Europe using nitrate wet deposition monitoring networks, *Atmos. Chem. Phys.*, 24, 4569–4589, <https://doi.org/10.5194/acp-24-4569-2024>, 2024.
- Copernicus Sentinel-5P: TROPOMI Level 2 Formaldehyde Column Products (RPRO version 02.04.00), European Space Agency [data set], <https://doi.org/10.5270/S5P-tjlxfd2>, 2018a.
- Copernicus Sentinel-5P: TROPOMI Level 2 Nitrogen Dioxide Column Products (RPRO version 02.04.00), European Space Agency [data set], <https://doi.org/10.5270/S5P-s4ljg54>, 2018b.
- Copernicus Sentinel-5P: TROPOMI Level 2 Carbon Monoxide Products. Version 02, European Space Agency [data set], <https://doi.org/10.5270/S5P-bj3nry0>, 2021.
- Crippa, M., Oreggioni, G., Guizzardi, D., Muntean, M., Schaaf, E., Lo Vullo, E., Solazzo, E., Monforti-Ferrario, F., Olivier, J., and Vignati, E.: Fossil CO<sub>2</sub> and GHG Emissions of All World Countries, Publications Office of the European Union, Luxembourg (Luxembourg), <https://doi.org/10.2760/687800>, 2019.
- Danabasoglu, G., Lamarque, J.-F., Bacmeister, J., Bailey, D. A., DuVivier, A. K., Edwards, J., Emmons, L. K., Fasullo, J., Garcia, R., Gettelman, A., Hannay, C., Holland, M. M., Large, W. G., Lauritzen, P. H., Lawrence, D. M., Lenaerts, J. T. M., Lindsay, K., Lipscomb, W. H., Mills, M. J., Neale, R., Ole-

- son, K. W., Otto-Bliesner, B., Phillips, A. S., Sacks, W., Tilmes, S., van Kampenhout, L., Vertenstein, M., Bertini, A., Dennis, J., Deser, C., Fischer, C., Fox-Kemper, B., Kay, J. E., Kinnison, D., Kushner, P. J., Larson, V. E., Long, M. C., Mickelson, S., Moore, J. K., Nienhouse, E., Polvani, L., Rasch, P. J., and Strand, W. G.: The Community Earth System Model Version 2 (CESM2), *J. Adv. Model. Earth Sy.*, 12, e2019MS001916, <https://doi.org/10.1029/2019MS001916>, 2020.
- Davis, N. A., Callaghan, P., Simpson, I. R., and Tilmes, S.: Specified dynamics scheme impacts on wave-mean flow dynamics, convection, and tracer transport in CESM2 (WACCM6), *Atmos. Chem. Phys.*, 22, 197–214, <https://doi.org/10.5194/acp-22-197-2022>, 2022.
- Dedoussi, I. C., Eastham, S. D., Monier, E., and Barrett, S. R. H.: Premature Mortality Related to United States Cross-State Air Pollution, *Nature*, 578, 261–265, <https://doi.org/10.1038/s41586-020-1983-8>, 2020.
- Di, Q., Wang, Y., Zanobetti, A., Wang, Y., Koutrakis, P., Choirat, C., Dominici, F., and Schwartz, J. D.: Air Pollution and Mortality in the Medicare Population, *New Engl. J. Med.*, 376, 2513–2522, <https://doi.org/10.1056/NEJMoa1702747>, 2017a.
- Di, Q., Dai, L., Wang, Y., Zanobetti, A., Choirat, C., Schwartz, J. D., and Dominici, F.: Association of Short-term Exposure to Air Pollution With Mortality in Older Adults, *JAMA*, 318, 2446–2456, <https://doi.org/10.1001/jama.2017.17923>, 2017b.
- Edwards, D. P., Martínez-Alonso, S., Jo, D. S., Ortega, I., Emmons, L. K., Orlando, J. J., Worden, H. M., Kim, J., Lee, H., Park, J., and Hong, H.: Quantifying the diurnal variation in atmospheric NO<sub>2</sub> from Geostationary Environment Monitoring Spectrometer (GEMS) observations, *Atmos. Chem. Phys.*, 24, 8943–8961, <https://doi.org/10.5194/acp-24-8943-2024>, 2024.
- Emmons, L. K., Schwantes, R. H., Orlando, J. J., Tyndall, G., Kinnison, D., Lamarque, J. F., Marsh, D., Mills, M. J., Tilmes, S., Bardeen, C., Buchholz, R. R., Conley, A., Gettelman, A., Garcia, R., Simpson, I., Blake, D. R., Meinardi, S., and Pétron, G.: The Chemistry Mechanism in the Community Earth System Model Version 2 (CESM2), *J. Adv. Model. Earth Sy.*, 12, 1–21, <https://doi.org/10.1029/2019MS001882>, 2020.
- Eskes, H. J., Basart, S., Benedictow, A., Bonna, Y., Blechschmidt, A.-M., Chabrillat, S., Christoph, Y., Cuevas, E., Flentje, H., Hansen, K. M., Kapsomenakis, J., Langerock, B., Ramonet, M., Richter, A., Schulz, M., Sudarchikova, N., Wagner, A., Warneke, T., and Zerefos, C.: Observation characterisation and validation methods document, Copernicus Atmosphere Monitoring Service (CAMS) report, <https://doi.org/10.24380/7cjp-dn95>, 2021.
- Fiore, A. M., Dentener, F. J., Wild, O., Cuvelier, C., Schultz, M. G., Hess, P., Textor, C., Schulz, M., Doherty, R. M., Horowitz, L. W., MacKenzie, I. A., Sanderson, M. G., Shindell, D. T., Stevenson, D. S., Szopa, S., Van Dingenen, R., Zeng, G., Atherton, C., Bergmann, D., Bey, I., Carmichael, G., Collins, W. J., Duncan, B. N., Faluvegi, G., Folberth, G., Gauss, M., Gong, S., Hauglustaine, D., Holloway, T., Isaksen, I. S. A., Jacob, D. J., Jonson, J. E., Kaminski, J. W., Keating, T. J., Lupu, A., Marmor, E., Montanaro, V., Park, R. J., Pitari, G., Pringle, K. J., Pyle, J. A., Schroeder, S., Vivanco, M. G., Wind, P., Wojcik, G., Wu, S., and Zuber, A.: Multimodel Estimates of Intercontinental Source-Receptor Relationships for Ozone Pollution, *J. Geophys. Res.-Atmos.*, 114, <https://doi.org/10.1029/2008JD010816>, 2009.
- Gao, Y., Wu, Y., Guo, X., Kou, W., Zhang, S., Leung, L. R., Chen, X., Lu, J., Diffenbaugh, N. S., Horton, D. E., Yao, X., Gao, H., and Wu, L.: More Frequent and Persistent Heatwaves Due To Increased Temperature Skewness Projected by a High-Resolution Earth System Model, *Geophys. Res. Lett.*, 50, e2023GL105840, <https://doi.org/10.1029/2023GL105840>, 2023.
- Gaubert, B., Emmons, L. K., Raeder, K., Tilmes, S., Miyazaki, K., Arellano Jr., A. F., Elguindi, N., Granier, C., Tang, W., Barré, J., Worden, H. M., Buchholz, R. R., Edwards, D. P., Franke, P., Anderson, J. L., Saunio, M., Schroeder, J., Woo, J.-H., Simpson, I. J., Blake, D. R., Meinardi, S., Wennberg, P. O., Crouse, J., Teng, A., Kim, M., Dickerson, R. R., He, H., Ren, X., Pusede, S. E., and Diskin, G. S.: Correcting model biases of CO in East Asia: impact on oxidant distributions during KORUS-AQ, *Atmos. Chem. Phys.*, 20, 14617–14647, <https://doi.org/10.5194/acp-20-14617-2020>, 2020.
- Geddes, J. A., Pusede, S. E., and Wong, A. Y. H.: Changes in the Relative Importance of Biogenic Isoprene and Soil NO<sub>x</sub> Emissions on Ozone Concentrations in Nonattainment Areas of the United States, *J. Geophys. Res.-Atmos.*, 127, e2021JD036361, <https://doi.org/10.1029/2021JD036361>, 2022.
- Gelaro, R., McCarty, W., Suárez, M. J., Todling, R., Molod, A., Takacs, L., Randles, C. A., Darmenov, A., Bosilovich, M. G., Reichle, R., Wargan, K., Coy, L., Cullather, R., Draper, C., Akella, S., Buchard, V., Conaty, A., da Silva, A. M., Gu, W., Kim, G. K., Koster, R., Lucchesi, R., Merkova, D., Nielsen, J. E., Parityka, G., Pawson, S., Putman, W., Rienecker, M., Schubert, S. D., Sienkiewicz, M., and Zhao, B.: The modern-era retrospective analysis for research and applications, version 2 (MERRA-2), *J. Climate*, 30, 5419–5454, <https://doi.org/10.1175/JCLI-D-16-0758.1>, 2017.
- Goldberg, D. L., Saide, P. E., Lamsal, L. N., de Foy, B., Lu, Z., Woo, J.-H., Kim, Y., Kim, J., Gao, M., Carmichael, G., and Streets, D. G.: A top-down assessment using OMI NO<sub>2</sub> suggests an underestimate in the NO<sub>x</sub> emissions inventory in Seoul, South Korea, during KORUS-AQ, *Atmos. Chem. Phys.*, 19, 1801–1818, <https://doi.org/10.5194/acp-19-1801-2019>, 2019.
- Goto, D., Sato, Y., Yashiro, H., Suzuki, K., Oikawa, E., Kudo, R., Nagao, T. M., and Nakajima, T.: Global aerosol simulations using NICAM.16 on a 14 km grid spacing for a climate study: improved and remaining issues relative to a lower-resolution model, *Geosci. Model Dev.*, 13, 3731–3768, <https://doi.org/10.5194/gmd-13-3731-2020>, 2020.
- Granier, C., Lamarque, J. F., Mieville, A., Muller, J. F., Olivier, J., Orlando, J., Peters, J., Petron, G., Tyndall, G., and Wallens, S.: POET, a database of surface emissions of ozone precursors, Institut Pierre-Simon Laplace, <http://www.aero.jussieu.fr/projet/ACCENT/POET.php> (last access: 17 July 2023), 2005.
- Guenther, A. B., Jiang, X., Heald, C. L., Sakulyanontvittaya, T., Duhl, T., Emmons, L. K., and Wang, X.: The Model of Emissions of Gases and Aerosols from Nature version 2.1 (MEGAN2.1): an extended and updated framework for modeling biogenic emissions, *Geosci. Model Dev.*, 5, 1471–1492, <https://doi.org/10.5194/gmd-5-1471-2012>, 2012.
- Guevara, M., Colette, A., Guion, A., Petiot, V., Adani, M., Arteta, J., Benedictow, A., Bergström, R., Bolignano, A., Camps, P., Carvalho, A. C., Christensen, J. H., Couvidat, F., D'Elia, I., Denier van der Gon, H., Descombes, G., Douros, J., Fagerli, H., Fatahi, Y., Friese, E., Frohn, L., Gauss, M., Geels, C., Hänenen, R.,

- Hansen, K., Jorba, O., Kaminski, J. W., Kouznetsov, R., Kranenburg, R., Kuenen, J., Lannuque, V., Meleux, F., Nyíri, A., Palamarchuk, Y., Pérez García-Pando, C., Robertson, L., Russo, F., Segers, A., Sofiev, M., Struzewska, J., Timmermans, R., Uppstu, A., Valdebenito, A., and Ye, Z.: Technical note: sensitivity of the CAMS regional air quality modelling system to anthropogenic emission temporal variability, *Atmos. Chem. Phys.*, 25, 13245–13278, <https://doi.org/10.5194/acp-25-13245-2025>, 2025.
- Holtzlag, A. A. M., Svensson, G., Baas, P., Basu, S., Beare, B., Beljaars, A. C. M., Bosveld, F. C., Cuxart, J., Lindvall, J., Steeneveld, G. J., Tjernström, M., and Van De Wiel, B. J. H.: Stable Atmospheric Boundary Layers and Diurnal Cycles: Challenges for Weather and Climate Models, *B. Am. Meteorol. Soc.*, 94, 1691–1706, <https://doi.org/10.1175/BAMS-D-11-00187.1>, 2013.
- Jo, D. S., Emmons, L. K., Callaghan, P., Tilmes, S., Woo, J.-H., Kim, Y., Kim, J., Granier, C., Soulié, A., Doumbia, T., Daras, S., Buchholz, R. R., Simpson, I. J., Blake, D. R., Wisthaler, A., Schroeder, J. R., Fried, A., and Kanaya, Y.: Comparison of Urban Air Quality Simulations During the KORUS-AQ Campaign With Regionally Refined Versus Global Uniform Grids in the Multi-Scale Infrastructure for Chemistry and Aerosols (MUSICA) Version 0, *J. Adv. Model. Earth Sy.*, 15, e2022MS003458, <https://doi.org/10.1029/2022MS003458>, 2023.
- Keller, C. A., Long, M. S., Yantosca, R. M., Da Silva, A. M., Pawson, S., and Jacob, D. J.: HEMCO v1.0: a versatile, ESMF-compliant component for calculating emissions in atmospheric models, *Geosci. Model Dev.*, 7, 1409–1417, <https://doi.org/10.5194/gmd-7-1409-2014>, 2014.
- Kleinman, L. I.: Low and High NO<sub>x</sub> Tropospheric Photochemistry, *J. Geophys. Res.*, 99, 831–838, <https://doi.org/10.1029/94jd01028>, 1994.
- Kleinman, L. I.: The dependence of tropospheric ozone production rate on ozone precursors, *Atmos. Environ.*, 39, 575–586, <https://doi.org/10.1016/j.atmosenv.2004.08.047>, 2005.
- Krol, M., Houweling, S., Bregman, B., van den Broek, M., Segers, A., van Velthoven, P., Peters, W., Dentener, F., and Bergamaschi, P.: The two-way nested global chemistry-transport zoom model TM5: algorithm and applications, *Atmos. Chem. Phys.*, 5, 417–432, <https://doi.org/10.5194/acp-5-417-2005>, 2005.
- Lamsal, L. N., Martin, R. V., Padmanabhan, A., van Donkelaar, A., Zhang, Q., Sioris, C. E., Chance, K., Kurosu, T. P., and Newchurch, M. J.: Application of Satellite Observations for Timely Updates to Global Anthropogenic NO<sub>x</sub> Emission Inventories, *Geophys. Res. Lett.*, 38, <https://doi.org/10.1029/2010GL046476>, 2011.
- Lamsal, L. N., Krotkov, N. A., Celarier, E. A., Swartz, W. H., Pickering, K. E., Bucsela, E. J., Gleason, J. F., Martin, R. V., Philip, S., Irie, H., Cede, A., Herman, J., Weinheimer, A., Szykman, J. J., and Knepp, T. N.: Evaluation of OMI operational standard NO<sub>2</sub> column retrievals using in situ and surface-based NO<sub>2</sub> observations, *Atmos. Chem. Phys.*, 14, 11587–11609, <https://doi.org/10.5194/acp-14-11587-2014>, 2014.
- Lange, K., Richter, A., Schönhardt, A., Meier, A. C., Bösch, T., Seyler, A., Krause, K., Behrens, L. K., Wittrock, F., Merlaud, A., Tack, F., Fayt, C., Friedrich, M. M., Dimitropoulou, E., Van Roozendaal, M., Kumar, V., Donner, S., Dörner, S., Lauster, B., Razi, M., Borger, C., Uhlmannsiek, K., Wagner, T., Ruhtz, T., Eskes, H., Bohn, B., Santana Diaz, D., Abuhassan, N., Schüttemeyer, D., and Burrows, J. P.: Validation of Sentinel-5P TROPOMI tropospheric NO<sub>2</sub> products by comparison with NO<sub>2</sub> measurements from airborne imaging DOAS, ground-based stationary DOAS, and mobile car DOAS measurements during the S5P-VAL-DE-Ruhr campaign, *Atmos. Meas. Tech.*, 16, 1357–1389, <https://doi.org/10.5194/amt-16-1357-2023>, 2023.
- Lawrence, D. M., Fisher, R. A., Koven, C. D., Oleson, K. W., Swenson, S. C., Bonan, G., Collier, N., Ghimire, B., van Kampenhout, L., Kennedy, D., Kluzek, E., Lawrence, P. J., Li, F., Li, H., Lombardozzi, D., Riley, W. J., Sacks, W. J., Shi, M., Vertenstein, M., Wieder, W. R., Xu, C., Ali, A. A., Badger, A. M., Bisht, G., van den Broeke, M., Brunke, M. A., Burns, S. P., Buzan, J., Clark, M., Craig, A., Dahlin, K., Drewniak, B., Fisher, J. B., Flanner, M., Fox, A. M., Gentine, P., Hoffman, F., Keppel-Aleks, G., Knox, R., Kumar, S., Lenaerts, J., Leung, L. R., Lipscomb, W. H., Lu, Y., Pandey, A., Pelletier, J. D., Perket, J., Randerson, J. T., Ricciuto, D. M., Sanderson, B. M., Slater, A., Subin, Z. M., Tang, J., Thomas, R. Q., Val Martin, M., and Zeng, X.: The Community Land Model Version 5: Description of New Features, Benchmarking, and Impact of Forcing Uncertainty, *J. Adv. Model. Earth Sy.*, 11, 4245–4287, <https://doi.org/10.1029/2018MS001583>, 2019.
- Lin, H., Jacob, D. J., Lundgren, E. W., Sulprizio, M. P., Keller, C. A., Fritz, T. M., Eastham, S. D., Emmons, L. K., Campbell, P. C., Baker, B., Saylor, R. D., and Montuoro, R.: Harmonized Emissions Component (HEMCO) 3.0 as a versatile emissions component for atmospheric models: application in the GEOS-Chem, NASA GEOS, WRF-GC, CESM2, NOAA GEFS-Aerosol, and NOAA UFS models, *Geosci. Model Dev.*, 14, 5487–5506, <https://doi.org/10.5194/gmd-14-5487-2021>, 2021.
- Makar, P. A., Staebler, R. M., Akingunola, A., Zhang, J., McLinden, C., Kharol, S. K., Pabla, B., Cheung, P., and Zheng, Q.: The Effects of Forest Canopy Shading and Turbulence on Boundary Layer Ozone, *Nat. Commun.*, 8, 15243, <https://doi.org/10.1038/ncomms15243>, 2017.
- Martin, R. V., Jacob, D. J., Chance, K., Kurosu, T. P., Palmer, P. I., and Evans, M. J.: Global Inventory of Nitrogen Oxide Emissions Constrained by Space-Based Observations of NO<sub>2</sub> Columns, *J. Geophys. Res.-Atmos.*, 108, <https://doi.org/10.1029/2003JD003453>, 2003.
- Martin, V. M., Heald, C. L., and Arnold, S. R.: Coupling Dry Deposition to Vegetation Phenology in the Community Earth System Model: Implications for the Simulation of Surface O<sub>3</sub>, *Geophys. Res. Lett.*, 41, 2988–2996, <https://doi.org/10.1002/2014GL059651>, 2014.
- McDuffie, E. E., Smith, S. J., O'Rourke, P., Tibrewal, K., Venkataraman, C., Marais, E. A., Zheng, B., Crippa, M., Brauer, M., and Martin, R. V.: A global anthropogenic emission inventory of atmospheric pollutants from sector- and fuel-specific sources (1970–2017): an application of the Community Emissions Data System (CEDS), *Earth Syst. Sci. Data*, 12, 3413–3442, <https://doi.org/10.5194/essd-12-3413-2020>, 2020.
- Meinshausen, M., Vogel, E., Nauels, A., Lorbacher, K., Meinshausen, N., Etheridge, D. M., Fraser, P. J., Montzka, S. A., Rayner, P. J., Trudinger, C. M., Krummel, P. B., Beyerle, U., Canadell, J. G., Daniel, J. S., Enting, I. G., Law, R. M., Lunder, C. R., O'Doherty, S., Prinn, R. G., Reimann, S., Rubino, M., Velders, G. J. M., Vollmer, M. K., Wang, R. H. J., and Weiss, R.: Historical greenhouse gas concentrations for cli-

- mate modelling (CMIP6), *Geosci. Model Dev.*, 10, 2057–2116, <https://doi.org/10.5194/gmd-10-2057-2017>, 2017.
- Menut, L., Goussebaile, A., Bessagnet, B., Khvorostiyannov, D., and Ung, A.: Impact of Realistic Hourly Emissions Profiles on Air Pollutants Concentrations Modelled With CHIMERE, *Atmos. Environ.*, 49, 233–244, <https://doi.org/10.1016/j.atmosenv.2011.11.057>, 2012.
- Miyazaki, K. and Eskes, H.: Constraints on Surface NO<sub>x</sub> Emissions by Assimilating Satellite Observations of Multiple Species, *Geophys. Res. Lett.*, 40, 4745–4750, <https://doi.org/10.1002/grl.50894>, 2013.
- Myriokefalitakis, S., Daskalakis, N., Gkouvousis, A., Hilboll, A., van Noije, T., Williams, J. E., Le Sager, P., Huijnen, V., Houweling, S., Bergman, T., Nüß, J. R., Vrekoussis, M., Kanakidou, M., and Krol, M. C.: Description and evaluation of a detailed gas-phase chemistry scheme in the TM5-MP global chemistry transport model (r112), *Geosci. Model Dev.*, 13, 5507–5548, <https://doi.org/10.5194/gmd-13-5507-2020>, 2020.
- Naeger, A. R., Newchurch, M. J., Moore, T., Chance, K., Liu, X., Alexander, S., Murphy, K., and Wang, B.: Revolutionary Air-Pollution Applications from Future Tropospheric Emissions: Monitoring of Pollution (TEMPO) Observations, *B. Am. Meteorol. Soc.*, 102, E1735–E1741, <https://doi.org/10.1175/BAMS-D-21-0050.1>, 2021.
- National Center for Atmospheric Research (NCAR): Regridding Meteorological Data, GitHub [data set], [https://github.com/NCAR/IPT/tree/master/Meteorological\\_Reanalysis\\_Data](https://github.com/NCAR/IPT/tree/master/Meteorological_Reanalysis_Data), last access: 26 January 2022a.
- National Center for Atmospheric Research (NCAR): Regridding Emissions, GitHub [code], <https://github.com/NCAR/MUSICA-Tools> (last access: 8 May 2026), 2022b.
- Park, J., Hong, H., Lee, H., Kim, S.-W., Kim, J., Van Roozendaal, M., Fayt, C., Ahn, M.-H., Jacob, D. J., Seo, S., Kim, K.-M., Kim, D., Choi, W., Lee, W.-J., Lee, D.-W., Wagner, T., Richter, A., Krotkov, N. A., Lamsal, L. N., Ko, D. H., Lee, S. H., and Woo, J.-H.: Tropospheric Nitrogen Dioxide Levels Vary Diurnally in Asian Cities, *Commun. Earth Environ.*, 6, 389, <https://doi.org/10.1038/s43247-025-02272-7>, 2025.
- Pfister, G. G., Eastham, S. D., Arellano, A. F., Aumont, B., Barsanti, K. C., Barth, M. C., Conley, A., Davis, N. A., Emmons, L. K., Fast, J. D., Fiore, A. M., Gaubert, B., Goldhaber, S., Granier, C., Grell, G. A., Guevara, M., Henze, D. K., Hodzic, A., Liu, X., Marsh, D. R., Orlando, J. J., Plane, J. M. C., Polvani, L. M., Rosenlof, K. H., Steiner, A. L., Jacob, D. J., and Brasseur, G. P.: The multi-scale infrastructure for chemistry and aerosols (MUSICA), *B. Am. Meteorol. Soc.*, 101, E1743–E1760, <https://doi.org/10.1175/BAMS-D-19-0331.1>, 2020.
- Schwantes, R. H., Emmons, L. K., Orlando, J. J., Barth, M. C., Tyn-dall, G. S., Hall, S. R., Ullmann, K., St. Clair, J. M., Blake, D. R., Wisthaler, A., and Bui, T. P. V.: Comprehensive isoprene and terpene gas-phase chemistry improves simulated surface ozone in the southeastern US, *Atmos. Chem. Phys.*, 20, 3739–3776, <https://doi.org/10.5194/acp-20-3739-2020>, 2020.
- Schwantes, R. H., Lacey, F. G., Tilmes, S., Emmons, L. K., Lauritzen, P. H., Walters, S., Callaghan, P., Zarzycki, C. M., Barth, M. C., Jo, D. S., Bacmeister, J. T., Neale, R. B., Vitt, F., Kluzek, E., Roozitalab, B., Hall, S. R., Ullmann, K., Warneke, C., Peischl, J., Pollack, I. B., Flocke, F., Wolfe, G. M., Hanisco, T. F., Keutsch, F. N., Kaiser, J., Bui, T. P. V., Jimenez, J. L., Campuzano-Jost, P., Apel, E. C., Hornbrook, R. S., Hills, A. J., Yuan, B., and Wisthaler, A.: Evaluating the Impact of Chemical Complexity and Horizontal Resolution on Tropospheric Ozone Over the Conterminous US With a Global Variable Resolution Chemistry Model, *J. Adv. Model. Earth Sy.*, 14, e2021MS002889, <https://doi.org/10.1029/2021MS002889>, 2022.
- Shah, V., Jacob, D. J., Dang, R., Lamsal, L. N., Strode, S. A., Steenrod, S. D., Boersma, K. F., Eastham, S. D., Fritz, T. M., Thompson, C., Peischl, J., Bourgeois, I., Pollack, I. B., Nault, B. A., Cohen, R. C., Campuzano-Jost, P., Jimenez, J. L., Andersen, S. T., Carpenter, L. J., Sherwen, T., and Evans, M. J.: Nitrogen oxides in the free troposphere: implications for tropospheric oxidants and the interpretation of satellite NO<sub>2</sub> measurements, *Atmos. Chem. Phys.*, 23, 1227–1257, <https://doi.org/10.5194/acp-23-1227-2023>, 2023.
- Shen, Y., Jiang, F., Feng, S., Xia, Z., Zheng, Y., Lyu, X., Zhang, L., and Lou, C.: Increased Diurnal Difference of NO<sub>2</sub> Concentrations and Its Impact on Recent Ozone Pollution in Eastern China in Summer, *Sci. Total Environ.*, 858, 159767, <https://doi.org/10.1016/j.scitotenv.2022.159767>, 2023.
- Sillman, S.: Tropospheric Ozone and Photochemical Smog, *Treatise on Geochemistry*, 9, 407–431, <https://doi.org/10.1016/B008-043751-6/09053-8>, 2003.
- Sillman, S. and He, D.: Some theoretical results concerning O<sub>3</sub>–NO<sub>x</sub>–VOC chemistry and NO<sub>x</sub>–VOC indicators, *J. Geophys. Res.-Atmos.*, 107, ACH 26-1–ACH 26-15, <https://doi.org/10.1029/2001JD001123>, 2002.
- Silvern, R. F., Jacob, D. J., Travis, K. R., Sherwen, T., Evans, M. J., Cohen, R. C., Laughner, J. L., Hall, S. R., Ullmann, K., Crouse, J. D., Wennberg, P. O., Peischl, J., and Pollack, I. B.: Observed NO/NO<sub>2</sub> Ratios in the Upper Troposphere Imply Errors in NO–NO<sub>2</sub>–O<sub>3</sub> Cycling Kinetics or an Unaccounted NO<sub>x</sub> Reservoir, *Geophys. Res. Lett.*, 45, 4466–4474, <https://doi.org/10.1029/2018GL077728>, 2018.
- Silvern, R. F., Jacob, D. J., Mickley, L. J., Sulprizio, M. P., Travis, K. R., Marais, E. A., Cohen, R. C., Laughner, J. L., Choi, S., Joiner, J., and Lamsal, L. N.: Using satellite observations of tropospheric NO<sub>2</sub> columns to infer long-term trends in US NO<sub>x</sub> emissions: the importance of accounting for the free tropospheric NO<sub>2</sub> background, *Atmos. Chem. Phys.*, 19, 8863–8878, <https://doi.org/10.5194/acp-19-8863-2019>, 2019.
- Soulie, A., Granier, C., Darras, S., Zilbermann, N., Doumbia, T., Guevara, M., Jalkanen, J.-P., Keita, S., Liousse, C., Crippa, M., Guizzardi, D., Hoesly, R., and Smith, S. J.: Global anthropogenic emissions (CAM5-GLOB-ANT) for the Copernicus Atmosphere Monitoring Service simulations of air quality forecasts and reanalyses, *Earth Syst. Sci. Data*, 16, 2261–2279, <https://doi.org/10.5194/essd-16-2261-2024>, 2024.
- Stjern, C. W., Hodnebrog, Ø., Myhre, G., and Pisso, I.: The Turbulent Future Brings a Breath of Fresh Air, *Nat. Commun.*, 14, 3735, <https://doi.org/10.1038/s41467-023-39298-4>, 2023.
- Strosnider, H. M., Chang, H. H., Darrow, L. A., Liu, Y., Vaidyanathan, A., and Strickland, M. J.: Age-specific associations of ozone and fine particulate matter with respiratory emergency department visits in the United States, *Am. J. Resp. Crit. Care*, 199, 882–890, <https://doi.org/10.1164/rccm.201806-1147OC>, 2019.

- Tang, W., Emmons, L. K., Buchholz, R. R., Wiedinmyer, C., Schwantes, R. H., He, C., Kumar, R., Pfister, G. G., Worden, H. M., Hornbrook, R. S., Apel, E. C., Tilmes, S., Gaubert, B., Martinez-Alonso, S.-E., Lacey, F., Holmes, C. D., Diskin, G. S., Bourgeois, I., Peischl, J., Ryerson, T. B., Hair, J. W., Weinheimer, A. J., Montzka, D. D., Tyndall, G. S., and Campos, T. L.: Effects of Fire Diurnal Variation and Plume Rise on U.S. Air Quality During FIREX-AQ and WE-CAN Based on the Multi-Scale Infrastructure for Chemistry and Aerosols (MUSICAv0), *J. Geophys. Res.-Atmos.*, 127, e2022JD036650, <https://doi.org/10.1029/2022JD036650>, 2022.
- Tang, W., Emmons, L. K., Worden, H. M., Kumar, R., He, C., Gaubert, B., Zheng, Z., Tilmes, S., Buchholz, R. R., Martinez-Alonso, S.-E., Granier, C., Soulie, A., McKain, K., Daube, B. C., Peischl, J., Thompson, C., and Levelt, P.: Application of the Multi-Scale Infrastructure for Chemistry and Aerosols version 0 (MUSICAv0) for air quality research in Africa, *Geosci. Model Dev.*, 16, 6001–6028, <https://doi.org/10.5194/gmd-16-6001-2023>, 2023a.
- Tang, W., Pfister, G. G., Kumar, R., Barth, M., Edwards, D. P., Emmons, L. K., and Tilmes, S.: Capturing High-Resolution Air Pollution Features Using the Multi-Scale Infrastructure for Chemistry and Aerosols Version 0 (MUSICAv0) Global Modeling System, *J. Geophys. Res.-Atmos.*, 128, e2022JD038345, <https://doi.org/10.1029/2022JD038345>, 2023b.
- Tang, W., Emmons, L. K., Wiedinmyer, C., Partha, D. B., Huang, Y., He, C., Zhang, J., Barsanti, K. C., Gaubert, B., Jo, D. S., Zhang, J., Buchholz, R., Tilmes, S., Vitt, F., Granier, C., Worden, H. M., and Levelt, P. F.: Disproportionately Large Impacts of Wildland-Urban Interface Fire Emissions on Global Air Quality and Human Health, *Sci. Adv.*, 11, eadr2616, <https://doi.org/10.1126/sciadv.adr2616>, 2025.
- Tao, M., Fiore, A. M., Jin, X., Schiferl, L. D., Commane, R., Judd, L. M., Janz, S., Sullivan, J. T., Miller, P. J., Karambelas, A., Davis, S., Tzortziou, M., Valin, L., Whitehill, A., Civerolo, K., and Tian, Y.: Investigating Changes in Ozone Formation Chemistry during Summertime Pollution Events over the Northeastern United States, *Environ. Sci. Technol.*, 56, 15312–15327, <https://doi.org/10.1021/acs.est.2c02972>, 2022.
- Tao, M., Fiore, A. M., Karambelas, A., Miller, P. J., Valin, L. C., Judd, L. M., Tzortziou, M., Whitehill, A., Teora, A., Tian, Y., Civerolo, K. L., Tong, D., Ma, S., Adamo, S. B., and Holloway, T.: Insights Into Summertime Surface Ozone Formation From Diurnal Variations in Formaldehyde and Nitrogen Dioxide Along a Transect Through New York City, *J. Geophys. Res.-Atmos.*, 130, e2024JD040922, <https://doi.org/10.1029/2024JD040922>, 2025.
- Tilmes, S., Hodzic, A., Emmons, L. K., Mills, M. J., Gettelman, A., Kinnison, D. E., Park, M., Lamarque, J.-F., Vitt, F., Shrivastava, M., Campuzano-Jost, P., Jimenez, J. L., and Liu, X.: Climate Forcing and Trends of Organic Aerosols in the Community Earth System Model (CESM2), *J. Adv. Model. Earth Sy.*, 11, 4323–4351, <https://doi.org/10.1029/2019MS001827>, 2019.
- Tonnesen, G. S. and Dennis, R. L.: Analysis of Radical Propagation Efficiency to Assess Ozone Sensitivity to Hydrocarbons and NO<sub>x</sub> 1. Local Indicators of Instantaneous Odd Oxygen Production Sensitivity, *J. Geophys. Res.-Atmos.*, 105, 9213–9225, <https://doi.org/10.1029/1999JD900371>, 2000.
- Travis, K. R., Jacob, D. J., Fisher, J. A., Kim, P. S., Marais, E. A., Zhu, L., Yu, K., Miller, C. C., Yantosca, R. M., Sulprizio, M. P., Thompson, A. M., Wennberg, P. O., Crounse, J. D., St. Clair, J. M., Cohen, R. C., Laughner, J. L., Dibb, J. E., Hall, S. R., Ullmann, K., Wolfe, G. M., Pollack, I. B., Peischl, J., Neuman, J. A., and Zhou, X.: Why do models overestimate surface ozone in the Southeast United States?, *Atmos. Chem. Phys.*, 16, 13561–13577, <https://doi.org/10.5194/acp-16-13561-2016>, 2016.
- U.S. Environmental Protection Agency (EPA): 2017 National Emissions Inventory (NEI) Data, US EPA [data set], <https://www.epa.gov/air-emissions-inventories/2017-national-emissions-inventory-nei-data>, last access: 25 January 2022.
- U.S. Environmental Protection Agency (EPA): Air Quality System (AQS) Pre-generated Data Files, US EPA [data set], [https://aq5.epa.gov/aqsweb/airdata/download\\_files.html](https://aq5.epa.gov/aqsweb/airdata/download_files.html), last access: 1 August 2023.
- U.S. Environmental Protection Agency (EPA): Hazardous Air Pollutants, <https://www.epa.gov/haps>, last access: 23 January 2024.
- van Geffen, J., Boersma, K. F., Eskes, H., Sneep, M., ter Linden, M., Zara, M., and Veefkind, J. P.: SSP TROPOMI NO<sub>2</sub> slant column retrieval: method, stability, uncertainties and comparisons with OMI, *Atmos. Meas. Tech.*, 13, 1315–1335, <https://doi.org/10.5194/amt-13-1315-2020>, 2020.
- van Geffen, J., Eskes, H., Compernelle, S., Pinardi, G., Verhoelst, T., Lambert, J.-C., Sneep, M., ter Linden, M., Ludewig, A., Boersma, K. F., and Veefkind, J. P.: Sentinel-5P TROPOMI NO<sub>2</sub> retrieval: impact of version v2.2 improvements and comparisons with OMI and ground-based data, *Atmos. Meas. Tech.*, 15, 2037–2060, <https://doi.org/10.5194/amt-15-2037-2022>, 2022.
- Wang, J. X. L. and Angell, J. K.: Air Stagnation Climatology for the United States (1948–1998), NOAA/Air Resources Laboratory ATLAS, no. 1, Air Resources Laboratory, <https://repository.library.noaa.gov/view/noaa/50572> (last access: 14 February 2026), 1999.
- Wang, Y. X., McElroy, M. B., Jacob, D. J., and Yantosca, R. M.: A Nested Grid Formulation for Chemical Transport Over Asia: Applications to CO, *J. Geophys. Res.-Atmos.*, 109, <https://doi.org/10.1029/2004JD005237>, 2004.
- Wiedinmyer, C., Kimura, Y., McDonald-Buller, E. C., Emmons, L. K., Buchholz, R. R., Tang, W., Seto, K., Joseph, M. B., Barsanti, K. C., Carlton, A. G., and Yokelson, R.: The Fire Inventory from NCAR version 2.5: an updated global fire emissions model for climate and chemistry applications, *Geosci. Model Dev.*, 16, 3873–3891, <https://doi.org/10.5194/gmd-16-3873-2023>, 2023.
- Williams, J. E., Boersma, K. F., Le Sager, P., and Verstraeten, W. W.: The high-resolution version of TM5-MP for optimized satellite retrievals: description and validation, *Geosci. Model Dev.*, 10, 721–750, <https://doi.org/10.5194/gmd-10-721-2017>, 2017.
- Wu, Y., Zhao, K., Ren, X., Dickerson, R. R., Huang, J., Schwab, M. J., Stratton, P. R., Daley, H., Li, D., and Moshary, F.: Ozone Pollution Episodes and PBL Height Variation in the NYC Urban and Coastal Areas During LISTOS 2019, *Atmos. Environ.*, 320, 120317, <https://doi.org/10.1016/j.atmosenv.2023.120317>, 2024.
- Yang, L. H., Jacob, D. J., Dang, R., Oak, Y. J., Lin, H., Kim, J., Zhai, S., Colombi, N. K., Pendergrass, D. C., Beaudry, E., Shah, V., Feng, X., Yantosca, R. M., Chong, H., Park, J., Lee, H., Lee, W.-J., Kim, S., Kim, E., Travis, K. R., Crawford, J. H., and Liao, H.: Interpreting Geostationary Environment Monitoring Spec-

- trometer (GEMS) geostationary satellite observations of the diurnal variation in nitrogen dioxide (NO<sub>2</sub>) over East Asia, *Atmos. Chem. Phys.*, 24, 7027–7039, <https://doi.org/10.5194/acp-24-7027-2024>, 2024.
- Yu, K., Jacob, D. J., Fisher, J. A., Kim, P. S., Marais, E. A., Miller, C. C., Travis, K. R., Zhu, L., Yantosca, R. M., Sulprizio, M. P., Cohen, R. C., Dibb, J. E., Fried, A., Mikoviny, T., Ryerson, T. B., Wennberg, P. O., and Wisthaler, A.: Sensitivity to grid resolution in the ability of a chemical transport model to simulate observed oxidant chemistry under high-isoprene conditions, *Atmos. Chem. Phys.*, 16, 4369–4378, <https://doi.org/10.5194/acp-16-4369-2016>, 2016.
- Zoogman, P., Liu, X., Suleiman, R. M., Pennington, W. F., Flittner, D. E., Al-Saadi, J. A., Hilton, B. B., Nicks, D. K., Newchurch, M. J., Carr, J. L., Janz, S. J., Andraschko, M. R., Arola, A., Baker, B. D., Canova, B. P., Chan Miller, C., Cohen, R. C., Davis, J. E., Dussault, M. E., Edwards, D. P., Fishman, J., Ghulam, A., González Abad, G., Grutter, M., Herman, J. R., Houck, J., Jacob, D. J., Joiner, J., Kerridge, B. J., Kim, J., Krotkov, N. A., Lamsal, L., Li, C., Lindfors, A., Martin, R. V, McElroy, C. T., McLinden, C., Natraj, V., Neil, D. O., Nowlan, C. R., O'Sullivan, E. J., Palmer, P. I., Pierce, R. B., Pippin, M. R., Saiz-Lopez, A., Spurr, R. J. D., Szykman, J. J., Torres, O., Veefkind, J. P., Veihelmann, B., Wang, H., Wang, J., and Chance, K.: Tropospheric emissions: Monitoring of pollution (TEMPO), *J. Quant. Spectrosc. Ra.*, 186, 17–39, <https://doi.org/10.1016/j.jqsrt.2016.05.008>, 2017.